A comparison of barostats for the mechanical characterisation of metal-organic frameworks

S.M.J. Rogge,[†] L. Vanduyfhuys,[†] A. Ghysels,[†] M. Waroquier,[†] T. Verstraelen,[†] G. Maurin,[‡] and V. Van Speybroeck[*,†]

Center for Molecular Modeling (CMM), Ghent University, Technologiepark 903, 9052 Zwijnaarde, Belgium, and Institut Charles Gerhardt Montpellier, Université Montpellier 2, Place Eugène Bataillon, 34095 Montpellier cedex 05, France

E-mail: Veronique.VanSpeybroeck@UGent.be

Abstract

In this paper, three barostat coupling schemes for pressure control, which are commonly used in molecular dynamics simulations, are critically compared to characterise the rigid MOF-5 and the flexible MIL-53(Al) metal-organic frameworks. We investigate the performance of the three barostats, the Berendsen, the Martyna-Tuckerman-Tobias-Klein (MTTK) and the Langevin coupling methods, in reproducing the cell parameters and the pressure versus volume behaviour in isothermal-isobaric simulations. A thermodynamic integration method is used to construct the free energy profiles as a function of volume at finite temperature. It is observed that the aforementioned static properties are well reproduced with the three barostats. However, for static properties depending nonlinearly on the pressure, the Berendsen barostat might give deviating results as it suppresses pressure fluctuations more drastically. Finally, dynamic properties, which

[*]To whom correspondence should be addressed
[†]Ghent University
[‡]Université Montpellier

are directly related to the fluctuations of the cell, such as the time to transition from the large-pore to the closed-pore phase, cannot be well reproduced by any of the coupling schemes.

1 Introduction

Molecular dynamics (MD) simulations have proven to be an indispensable tool in gaining insight in the microscopic behaviour of a broad range of materials, and are widely used to characterise, amongst others, biomolecules and nanoporous materials.[1–3] While the most basic MD algorithm solves Hamilton's classical equations of motion and predicts properties in the microcanonical ensemble,[4] most experiments are carried out under constant temperature and pressure. Hence, thermostat and barostat algorithms are introduced in the MD simulation to explicitly control the temperature and the pressure respectively. A variety of different algorithms exists, based on different equations of motion, to perturb the original system and to yield properties at constant temperature and/or pressure. However, these perturbations might lead to nonphysical artifacts, as was shown in recent critical assessments on the use of thermostats.[5–8] For barostats, prior work indicated that not all barostats predict the correct volume distribution function for isotropic systems,[9] but it was not further investigated how this affects the simulation results. Herein, such study is presented and a critical comparison is made of the influence of barostats on the properties of metal-organic frameworks.

Temperature control in MD simulations was initiated by Turq *et al.* in 1977, who applied the principle of Brownian motion to cool down a system, and so obtaining the Langevin equations.[10] These equations were later generalised by the group of Parrinello with the help of the canonical sampling through velocity rescaling (CSVR) thermostat [11–14] and colored-noise thermostat,[15–17] increasing both the efficiency and the applicability of the simulations. In addition, pioneering work was performed by Andersen, who introduced stochastic collisions to equilibrate the temperature,[18] and by Berendsen *et al.*, who proposed a completely deterministic method to control the temperature.[19] Another deterministic approach was also independently followed by Hoover *et al.*,[20] Evans and Morriss,[21] and Haile and Gupta,[22] whose ideas were combined in the so-called Nosé thermostat.[23,24] In this thermostat, Nosé introduced a unified formulation to control the temperature deterministically by extending the original system with an additional thermostat degree of freedom. This idea was refor-

mulated by Hoover, resulting in the well-known Nosé-Hoover thermostat,[25] and extended by Nosé allowing to couple differently to the various degrees of freedom of the system.[26] Martyna *et al.* introduced additional thermostat degrees of freedom in the so-called Nosé-Hoover chains,[27] which were recently extended to form Nosé-Hoover networks by Morishita.[28] While we will concentrate on the Langevin, Berendsen and Nosé-Hoover chain thermostat, it should be observed that the quest for new thermostats is still ongoing. Noteworthy results may be found in nonequilibrium simulations using dissipative particle dynamics,[29] faster equilibration techniques with the aid of log oscillators,[30] and advanced coupling methods between the thermostat and the original system.[31]

Likewise, a plethora of barostats exists, starting with the work of Parrinello and Rahman,[32,33] which was further explored by Nosé and Klein.[34] However, it was shown that the resulting equations of motion depend on the initial cell orientation, which is undesirable.[35,36] Independently, Andersen,[18] Berendsen *et al.*[19] and Hoover[25,37] developed deterministic barostats. The Hoover barostat was extended to account for fluctuations in both cell shape and volume by Melchionna *et al.*[38] It was later observed by Martyna *et al.* that the proposed equations of motion were only correct in the limit of large systems. To account for this, they introduced their own equations in the Martyna-Tuckerman-Tobias-Klein (MTTK) barostat,[39,40] which will be employed and tested in this work. Finally, the idea of the Langevin thermostat was extended to achieve pressure control, first by only scaling the volume of the system,[9] but later on by also allowing the cell shape to fluctuate.[41] Since these barostats affect the equations of motion, it is of the utmost importance to know the influence of the various coupling schemes on the prediction of properties for different materials.

In this work, we will use and compare three of these barostat implementations, the Berendsen, MTTK and Langevin barostat, for the simulation of metal-organic frameworks (MOFs), a specific class of nanoporous materials consisting of metal oxides interconnected by organic linkers. These materials are envisaged to play an important role in applications such as gas storage, separation, catalysis and controlled drug release.[42–45] While the synthesis of

MOFs started only two decades ago,[46–50] a continuously expanding set of MOFs is examined today to find the ideal candidate for the aforementioned applications.[51–57] However, for any of these applications, a mechanical characterisation of the MOF is a prerequisite. Indeed, before a MOF can be used as a porous catalyst material in a reactor, the MOF powder needs to be shaped, which involves pressures in the order of several GPa.[58] Moreover, flexible MOFs are also promising for the absorption of shocks or for the storage of other forms of mechanical energy because of their structural transitions at moderate pressures of several tens of MPa.[59–64] Hence, to aid their further development, a complete understanding of the mechanical behaviour of MOFs over a broad range of pressures is essential.

In this article, two prototype materials are highlighted. The first material, the highly flexible MIL-53(Al), consists of aluminium oxide chains, which are interconnected by benzenedicarboxylate linkers. This material exhibits two phases, the closed-pore (CP) and the large-pore (LP) phase, with a relative volume difference of 38% and belonging to a different symmetry group. For MIL-53 type materials, transitions between the two phases can be triggered by changing their relative stability through external parameters such as temperature,[64,65] pressure[59,63,64,66] and gas or liquid exposure.[55,56] Hence, MD simulations on MIL-53(Al) might critically depend on the applied thermostat and barostat. The second material at hand is MOF-5,[46] a rigid structure composed of zinc oxide centres and phenyl linkers. MOF-5 is renowned for its negative thermal expansion coefficient,[67] and its predicted bulk modulus is verified based on experimental and computational studies.[68,69]

MD simulations have proven to be an essential tool in the fundamental understanding of the structural behaviour of these solids upon diverse stimuli and of the dynamics of guest molecules confined into their pores. Ford *et al.* determined the self-diffusion of chain molecules in MOF-5,[70] while Rosenbach *et al.*, Salles *et al.*, and Babarao and Jiang studied diffusion of light hydrocarbons and CO_2 in MIL-47(V), MIL-53(Al) and MIL-53(Cr).[71–74] For MIL-53(Cr), Paesani also investigated the process of water-mediated proton transport.[75] All these theoretical investigations were carried out in the (N, V, T) ensemble with different

thermostat implementations, some of which were shown to give erronous results.[8] Several studies also report on MD simulations carried out in the (N,P,T) ensemble, such as the work of Greathouse *et al.* on the cell parameters of MOF-5 when immersed in water,[76] and the work of Tafipolsky and Schmid in a validation of a force-field development protocol for MOFs.[77] Further, (N,P,T) simulations have been performed by Yot *et al.* to investigate the breathing behaviour of MIL-47(V) and MIL-53(Al) under the influence of pressure,[59,62] as well as by Ghoufi and Maurin in their hybrid osmotic Monte Carlo scheme.[78] Except for the simulations in Ref. 76, where an MTTK barostat has been employed, all other works employ the Berendsen pressure coupling method. In order to reliably predict different properties of these challenging materials, it is necessary to compare and validate results obtained with different barostats. This is precisely the aim of this work. We will make a distinction between static properties, such as cell lengths and equilibrium geometries, and dynamic properties, such as the rate at which the aforementioned structural transitions occur.

This work is organised as follows. In Section 2, a more precise notation is introduced to describe various thermodynamic ensembles. Next, an overview of the three barostats in this work, the Berendsen, MTTK and Langevin barostat, is given with focus on the differences in their mechanism. Also, the methodology to derive the mechanical properties of interest is outlined. After stating the computational details in Section 3, the different barostats are applied in three distinct applications (Section 4). First, the reproduction of the unit cell parameters for the stable state of MOF-5 and the CP and LP structural phases in MIL-53(Al) is discussed with a selection of the relevant internal coordinates to characterise the structural transformation in MIL-53(Al) (Section 4.1). Second, internal pressure versus volume profiles are constructed. From these profiles, the transition pressure can be determined, and using a thermodynamic integration method, the free energy versus volume profiles may be constructed (Section 4.2). In a third application, the transition pressure is derived via a dynamical analysis in Section 4.3. Finally, in Section 5, concluding remarks are made concerning the use of the different barostats, which are especially relevant

when simulating metal-organic frameworks.

2 Theory

2.1 Thermodynamic ensembles

In order to fully describe the size and shape modifications of flexible materials such as MOFs, it is essential to introduce a unit cell tensor $\mathbf{h}$ that contains the three unit cell vectors $\boldsymbol{a}, \boldsymbol{b}$ and $\boldsymbol{c}$ as shown in Figure 1. The unit cell tensor can be split up in the cell volume $V = \det(\mathbf{h})$ and a normalised unit cell tensor $\mathbf{h}_0$ with $\det(\mathbf{h}_0) = 1$:

$$\mathbf{h} = V^{1/3}\mathbf{h}_0 \tag{2.1}$$

In the general three-dimensional case, the unit cell tensor $\mathbf{h}$ contains nine degrees of freedom. Three of them describe the orientation of the cell with respect to the chosen reference frame and are irrelevant for determining the physical properties of the system. Of the remaining six physical degrees of freedom, one is assigned to the volume, while the other five are contained in $\mathbf{h}_0$ and describe the shape of the unit cell.

An analogous separation can be applied to the external stress tensor $\boldsymbol{\sigma}$, which is assumed to be symmetric. Indeed, any asymmetry results in a global rotation of the unit cell, and thus yields no additional information. This symmetric tensor with six degrees of freedom consists of a hydrostatic pressure $P = \mathrm{Tr}\,(\boldsymbol{\sigma})/3$ and a deviatoric stress $\boldsymbol{\sigma}_a$ with the remaining five degrees of freedom [79]

$$\boldsymbol{\sigma} = P\mathbf{1} + \boldsymbol{\sigma}_a \tag{2.2}$$

with $\mathrm{Tr}\,(\boldsymbol{\sigma}_a) = 0$. It will be shown in the Methodology section that the isotropic and anisotropic contributions to the stress tensor result in a different material response.

These four thermodynamic quantities—$V, \mathbf{h}_0, P$ and $\boldsymbol{\sigma}_a$—can be used to define a variety of thermodynamic ensembles. In Table 1, an overview is given of the possible ensembles

Table 1: An overview of the different thermodynamic ensembles that can be considered when choosing the fixed boundary conditions from the number of particles N, the volume V, the normalised unit cell tensor $\mathbf{h}_0$, the average hydrostatic pressure $\langle P \rangle$, the average deviatoric stress $\langle \boldsymbol{\sigma}_a \rangle$, the generalised enthalpy E (or H), and the average temperature $\langle T \rangle$. For completeness, ensemble names which are conventionally used in standard MD software packages are included as well. The ensembles for which $\langle \boldsymbol{\sigma}_a \rangle = \mathbf{0}$ are special cases of the more general ensembles defined in the upper part of the table.

Ensemble	N	V	$\mathbf{h}_0$	$\langle P \rangle$	$\langle \boldsymbol{\sigma}_a \rangle$	E or H	$\langle T \rangle$	Commonly used notation
$NV(\mathbf{h}_0)E$	×	×	×			×		NVE[80–82]
$NV(\mathbf{h}_0)T$	×	×	×				×	NVT[80–82]
$NV(\boldsymbol{\sigma}_a)H$	×	×			×	×		
$NV(\boldsymbol{\sigma}_a)T$	×	×			×		×	
$NP(\mathbf{h}_0)H$	×		×	×		×		NPH,[80,81] NPE_I[82]
$NP(\mathbf{h}_0)T$	×		×	×			×	NPT,[80,81] NPT_I[82]
$NP(\boldsymbol{\sigma}_a)H$	×			×	×	×		NPH[81]
$NP(\boldsymbol{\sigma}_a)T$	×			×	×		×	NPT[81]
$NV(\boldsymbol{\sigma}_a = \mathbf{0})H$	×	×			$\langle \boldsymbol{\sigma}_a \rangle = \mathbf{0}$	×		
$NV(\boldsymbol{\sigma}_a = \mathbf{0})T$	×	×			$\langle \boldsymbol{\sigma}_a \rangle = \mathbf{0}$		×	
$NP(\boldsymbol{\sigma}_a = \mathbf{0})H$	×			×	$\langle \boldsymbol{\sigma}_a \rangle = \mathbf{0}$	×		$N\boldsymbol{\sigma}H$,[80] NPE_F[82]
$NP(\boldsymbol{\sigma}_a = \mathbf{0})T$	×			×	$\langle \boldsymbol{\sigma}_a \rangle = \mathbf{0}$		×	$N\boldsymbol{\sigma}T$,[80] NPT_F[82]

defined by fixing one or more of these four quantities, as well as the number of particles N, the total energy E or generalised enthalpy H, and the temperature T. The ensemble notation as used in common MD packages (DL_POLY,[80] lammps[81] and CP2K[82]) is shown in the third column of Table 1. These common names are not able to discriminate between all different thermodynamic ensembles. Hence, we need a decomposition of the unit cell and stress tensor into an isotropic and anisotropic part to unequivocally label the ensembles and assign the quantities which are kept constant. In the remainder of this paper, the extended notation that is proposed in the first column of Table 1 will be systematically adopted to avoid any confusion.

2.2 Barostats used to control the pressure

For this comparative study, three distinct barostats were considered and implemented in Yaff, our in-house developed software package for MD simulations.[83] We explicitly refer to this software package for the implementation, as it was shown that the choice of discretisation technique can influence the simulation outcome, even when starting from the same equations of motion.[84–86] An overview of the investigated barostats is given in Figure 1, in which the instantaneous pressure tensor $\mathbf{P}_i$ is defined as

$$\mathbf{P}_i = \frac{1}{V}\left[\sum_{j=1}^{N} \frac{\boldsymbol{p}_j \otimes \boldsymbol{p}_j}{m_j} - \boldsymbol{\Xi}\right] \tag{2.3}$$

In Eq. (2.3), V is the volume occupied by the system consisting of N particles with masses m_j and momenta $\boldsymbol{p}_j$, and $\boldsymbol{\Xi}$ is the virial tensor as defined in Section 1 of the Supporting Information. The instantaneous (scalar) pressure P_i is found as the average of the diagonal elements of the pressure tensor:

$$P_i = \frac{1}{3}\,\mathrm{Tr}\,(\mathbf{P}_i) \tag{2.4}$$

These definitions naturally emerge when considering a Hamiltonian derivation of the equations of motion for a system under conditions of a constant external pressure, as shown in Section 1 of the Supporting Information.

The aim of each barostat coupling method is to alter the instantaneous pressure tensor $\mathbf{P}_i$ such that on average the external stress $\boldsymbol{\sigma}$ is retrieved. Not only the method to achieve this condition differs for each barostat, but also with a given barostat implementation, different results can be obtained by tuning the influence of the barostat on the system. This last effect is quantified by the barostat relaxation time τ_P. This input parameter introduces a time scale for the system to respond to an external pressure. Hence, a low barostat relaxation time indicates a very aggressive barostat, which strongly interferes with the dynamics of the system. In the other limit, barostats with a high relaxation time influence the system much less abruptly, and the system will need more time to adapt to a new pressure condition. In

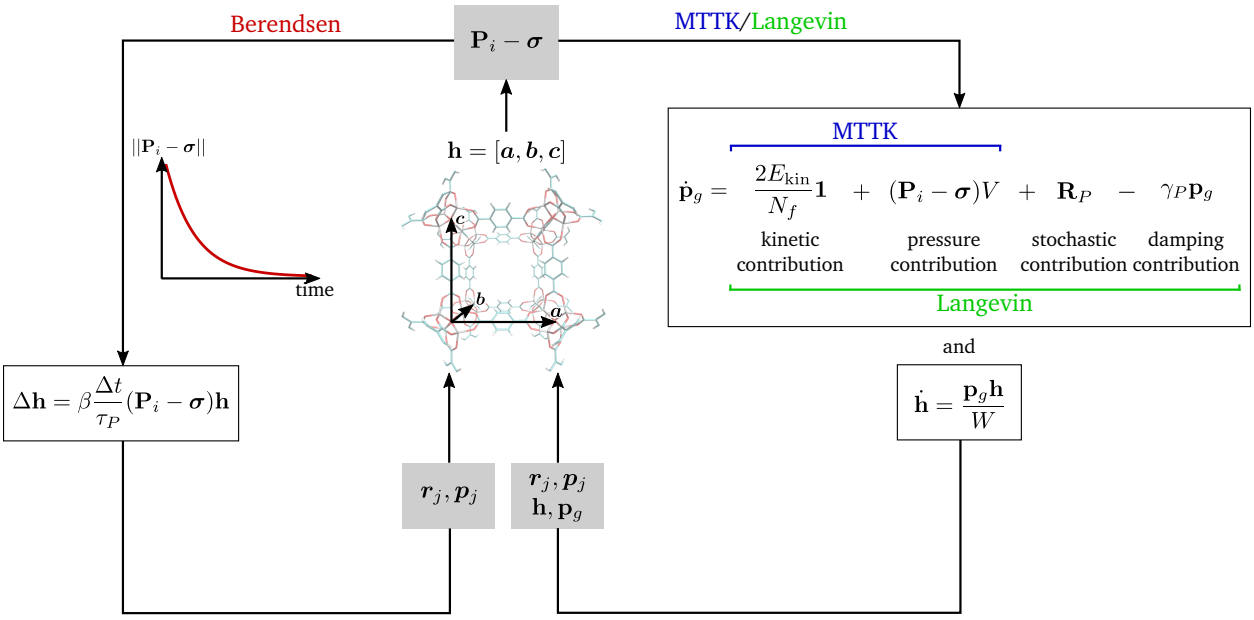

Figure 1: An overview of the different barostats compared in this work, and how they handle the pressure control via rescaling of the unit cell tensor $\mathbf{h}$. Some dependencies of the positions and momenta are omitted for clarity, as well as the effect of coupling to a thermostat. In this work, we always assume $\boldsymbol{\sigma}_a = \mathbf{0}$, and thus $\boldsymbol{\sigma} = P\mathbf{1}$.

the limit for $\tau_P \to \infty$, no pressure control is present.

The first barostat employed in this study was introduced by Berendsen and co-workers in 1984.[19] In their Berendsen barostat, both the positions $\boldsymbol{r}_j$ of the particles and the cell tensor $\mathbf{h}$ are rescaled at every integration step with the matrix $\boldsymbol{\mu} = \mathbf{1} + \beta(\mathbf{P}_i - \boldsymbol{\sigma})\Delta t/\tau_P$. Here, β is the isothermal compressibility. This step aims at an exponential damping of the difference between the instantaneous internal pressure $\mathbf{P}_i$ and the external stress $\boldsymbol{\sigma}$, as is shown in the left branch of Figure 1. However, this strong damping of the pressure difference $\mathbf{P}_i - \boldsymbol{\sigma}$ is unphysical, and disfavours strong fluctuations in both kinetic and potential energy. While the Berendsen barostat succeeds in imposing the average hydrostatic pressure P_i, it fails to retrieve the correct fluctuations of this instantaneous pressure, artificially reducing the variance of P_i, as shown below. An analogous technique is used in the Berendsen thermostat, for which it was shown that the resulting temperature distribution deviates from the theoretical distribution.[87]

The second barostat technique in this work is the algorithm proposed by Martyna, Tuckerman, Tobias and Klein, the MTTK barostat.[39,40] The method can be seen as the natural extension of the Nosé-Hoover and Nosé-Hoover chain thermostat.[25,27] In their barostat, a cell momentum tensor $\mathbf{p}_g$ is associated with the unit cell tensor $\mathbf{h}$, and drives the fluctuations of this unit cell tensor. The equations of motion of the cell momentum tensor $\mathbf{p}_g$ depend on both the kinetic energy E_{kin} and the difference between the desired isotropic stress tensor $\boldsymbol{\sigma} = P\mathbf{1}$ and the instantaneous pressure tensor $\mathbf{P}_i$ following

$$\dot{\mathbf{h}} = \frac{\mathbf{p}_g \mathbf{h}}{W} \tag{2.5a}$$

$$\dot{\mathbf{p}}_g = (\mathbf{P}_i - P\mathbf{1})V + \frac{2E_{\text{kin}}}{N_f}\mathbf{1} - \frac{p_\xi}{Q}\mathbf{p}_g \tag{2.5b}$$

The barostat mass W,

$$W = (N_f + 9)\frac{k_B T}{2}\left(\frac{\tau_P}{2\pi}\right)^2, \tag{2.6}$$

scales as the square of the barostat relaxation time τ_P, and N_f is the number of degrees of freedom in the system. The factor $k_B T$, with k_B Boltzmann's constant, introduces a natural energy scale. The last term in Eq. (2.5b) stems from the temperature control via a Nosé-Hoover thermostat with mass Q and thermostat momentum p_ξ. These equations of motion are shown in the right branch of Figure 1, where the temperature control term is not displayed for clarity. To be consistent with the required phase space distribution, the cell momentum tensor $\mathbf{p}_g$ should also enter in the equations of motion for the positions $\boldsymbol{r}_j$ and momenta $\boldsymbol{p}_j$ of the particles. The proof of the correctness of this algorithm, which is not straightforward, was carried out by Tuckerman *et al.* for the case of an isotropic pressure.[88] Thanks to the deterministic nature of the MTTK barostat, one can theoretically reverse time to propagate the system backwards. Furthermore, this method is characterised by a conserved energy, which proved to be a fast initial verification of the implementation.

The third barostat under consideration is the Langevin piston method,[9,41] which is based

on the Langevin thermostat.[10] As in the MTTK barostat, the unit cell tensor $\mathbf{h}$ has a cell momentum tensor $\mathbf{p}_g$ associated to it. The equations of motion resemble Eq. (2.5b), but an additional damping force $-\gamma_P \mathbf{p}_g$ and stochastic force $\mathbf{R}_P$ are introduced:

$$\dot{\mathbf{p}}_g = (\mathbf{P}_i - P\mathbf{1})V + \frac{2E_{\text{kin}}}{N_f}\mathbf{1} - \gamma_P \mathbf{p}_g + \mathbf{R}_P \tag{2.7}$$

with γ_P the damping coefficient, which is proportional to $1/\tau_P$. The magnitude of $\mathbf{R}_P$ is coupled with γ_P, and hence τ_P, through the fluctuation-dissipation theorem. These two new terms introduce a Brownian motion for the cell momentum tensor. Consequently, the system decorrelates faster in time, but the algorithm is no longer time-reversible. This barostat is represented in the right branch of Figure 1.

Despite their differences, the MTTK and Langevin barostat should yield the correct ensemble, in contrast to the Berendsen barostat. To illustrate this, the probability density function (PDF) of the instantaneous pressure P_i in an MD simulation of MIL-53(Al) is examined using the three barostats. The MD simulation is performed in the $(N, P, \boldsymbol{\sigma}_a = \mathbf{0}, T)$ ensemble for $P = 1$ MPa, $T = 300$ K and relaxation times of $\tau_T = 0.1$ ps for the thermostat and $\tau_P = 1.0$ ps for the barostat. The result of this comparison is displayed in the left pane of Figure 2, which shows that the MTTK and Langevin barostat yield the same pressure distribution, while the Berendsen barostat clearly disfavours large fluctuations in the internal pressure. Due to the large fluctuations for the MTTK and Langevin barostat, which can be up to 2000 times as large as the average instantaneous pressure $\langle P_i \rangle = 1$ MPa, the mean internal stress converges less quickly to the external stress. This might complicate the equilibration process, which is why the Berendsen barostat is often used during an initial equilibration. Also displayed, in the right pane of Figure 2, is the running average of the instantaneous pressure, defined as the moving average of the instantaneous pressure over the interval $[0, t]$. For all barostats, equilibration takes place within 1 ps, where the Langevin barostat is the fastest for this material.

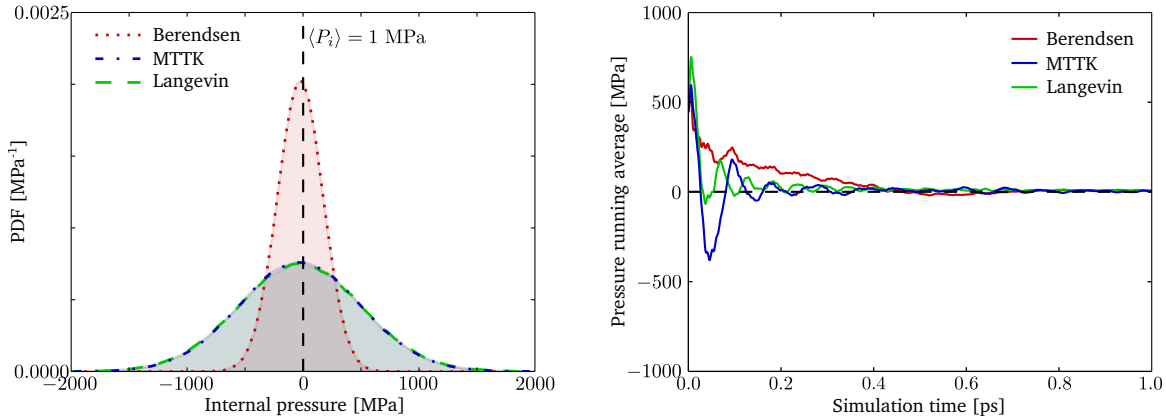

Figure 2: Internal pressure of MIL-53(Al) in a $(N, P, \boldsymbol{\sigma}_a = \mathbf{0}, T)$ simulation (1 MPa, 300 K) using the three barostats under study and starting from the metastable LP structure at 0 K. **Left:** Probability density function (PDF), generated over a simulation time of 800 ps. **Right:** Running average of the internal pressure, generated for the first picosecond.

2.3 Methodology for the mechanical characterisation of MOFs

As mentioned in the introduction, various properties will be derived from the MD simulations. For this, two types of ensembles will be used, which are outlined below.

2.3.1 The $(N, P, \boldsymbol{\sigma}_a = \mathbf{0}, T)$ ensemble for pressure responses

To assess the performance of the three barostats under consideration, MD simulations are carried out for the two metal-organic frameworks (MOF-5 and MIL-53(Al)) at 300 K and with an isotropic external pressure. These conditions fall under the category of a $(N, P, \boldsymbol{\sigma}_a = \mathbf{0}, T)$ ensemble (see Table 1). Several simulations have been performed with a pressure between 100 kPa and 1 GPa, starting from the optimised large-pore structure at 0 K for MIL-53(Al) or the global optimised structure at 0 K for MOF-5. For MOF-5, special attention is paid to the stability of the cell parameters and the internal geometry. For MIL-53(Al), it is investigated in which of the two states the system will reside during the simulation: the large pore (LP) or the closed pore (CP). The unit cell volume is here taken as criterion: when it crosses a threshold volume V_{tr}, we assume that a transition between the two phases has taken place. For MIL-53(Al), a threshold volume $V_{\mathrm{tr}} = 1000$ Å^3 is chosen, based on

the volumes of CP and LP structures obtained in earlier work.[59,65] For further analysis, we also define the time to transition $t_{\mathrm{LP}\to\mathrm{CP}}$ as the time needed for the system to undergo this LP-to-CP transition in an MD simulation starting from the LP phase (see Figure S.1):

$$t_{\mathrm{LP}\to\mathrm{CP}} = \min\{t | V_i(t) \leq V_{\mathrm{tr}}\} \tag{2.8}$$

2.3.2 The $(N, V, \boldsymbol{\sigma}_a = \mathbf{0}, T)$ ensemble for thermodynamic integration

While the $(N, P, \boldsymbol{\sigma}_a = \mathbf{0}, T)$ ensemble is the most used ensemble to describe materials under constant pressure, a new ensemble will be used to extract the free energy profile and derived properties, such as the transition pressure and the bulk modulus. This free energy profile is generated at a finite temperature, since it was shown that temperature plays an important role in determining the mechanical properties of MOFs.[89] For the determination of these mechanical quantities, we propose the use of the $(N, V, \boldsymbol{\sigma}_a = \mathbf{0}, T)$ ensemble. In this ensemble, the volume V and the deviatoric stress $\boldsymbol{\sigma}_a$ are kept fixed, while the cell shape and isotropic instantaneous pressure are not constrained. In practice, this ensemble can be derived from the MTTK barostat in Eq. (2.5). Indeed, the update of the cell volume V and the normalised unit cell tensor $\mathbf{h}_0$ can be completely separated. By using Eq. (2.1), the equations of motion may be rewritten as

$$\dot{V} = \frac{p_g V}{W_1} \tag{2.9a}$$

$$\dot{p}_g = 3V(P_i - P) + \frac{6E_{\mathrm{kin}}}{N_f} - \frac{p_\xi}{Q} p_g \tag{2.9b}$$

$$\dot{\mathbf{h}}_0 = \frac{\mathbf{p}_{g,0}\mathbf{h}_0}{W_2} \tag{2.9c}$$

$$\dot{\mathbf{p}}_{g,0} = V(\mathbf{P}_i - P\mathbf{1}) - \frac{V}{3}\mathrm{Tr}(\mathbf{P}_i - P\mathbf{1})\mathbf{1} - \frac{p_\xi}{Q}\mathbf{p}_{g,0}, \tag{2.9d}$$

where we replaced the full cell momentum tensor $\mathbf{p}_g$ by a scalar part p_g and a tensorial part $\mathbf{p}_{g,0}$ with $\mathrm{Tr}(\mathbf{p}_{g,0}) = 0$, which are decoupled. Moreover, instead of one barostat mass W in Eq.

(2.5a), two barostat masses W_1 and W_2 are introduced, which can be chosen independently.

Next, the instantaneous pressure is split into an isotropic and an anisotropic part as $\mathbf{P}_i = P_i\mathbf{1} + \boldsymbol{\sigma}_{i,a}$, similarly to Eq. (2.2). Eq. (2.9d) can then be rewritten as

$$\dot{\mathbf{p}}_{g,0} = V\boldsymbol{\sigma}_{i,a} - \frac{V}{3}\mathrm{Tr}(\boldsymbol{\sigma}_{i,a})\mathbf{1} - \frac{p_\xi}{Q}\mathbf{p}_{g,0} \tag{2.10}$$

which is completely independent of the isotropic pressure P. Hence, the equation of motion of $\mathbf{p}_{g,0}$, and thus also the equation of motion of the normalised unit cell tensor $\mathbf{h}_0$, only depends on the deviatoric internal stress $\boldsymbol{\sigma}_{i,a}$. Finally, we can choose $W_1 \to \infty$, in which case $\dot{V} = 0$: the cell volume is kept fixed. However, the cell shape can still fluctuate through the second set of equations, Eqs. (2.9c–2.9d), since W_2 remains finite. Hence, we finally arrive at the $(N, V, \boldsymbol{\sigma}_a = \mathbf{0}, T)$ ensemble. A similar procedure can be applied for the Berendsen and Langevin barostat, so that this new ensemble can be implemented for all three pressure coupling methods.

From the MD simulations in the $(N, V, \boldsymbol{\sigma}_a = \mathbf{0}, T)$ ensemble, the ensemble average of the instantaneous hydrostatic pressure $\langle P_i \rangle$ is measured. Our choice of ensemble ensures that the system can relax its structure under the sole constraint of a constant volume. Since the hydrostatic pressure is the negative volume derivative of the free energy, one can compute this free energy relative to some reference point via thermodynamic integration:[90]

$$F(V) - F(V_{\mathrm{ref}}) = \int_{V_{\mathrm{ref}}}^{V} \frac{\partial F(V')}{\partial V'}\mathrm{d}V' = -\int_{V_{\mathrm{ref}}}^{V} \langle P_i(V') \rangle \mathrm{d}V' \tag{2.11}$$

In practice, the integration is carried out by performing $(N, V, \boldsymbol{\sigma}_a = \mathbf{0}, T)$ MD simulations at a series of volumes in a closely spaced volume grid, to numerically approximate the integral of Eq. (2.11) by a finite sum. In this paper, the initial structures for these $(N, V, \boldsymbol{\sigma}_a = \mathbf{0}, T)$ simulations, which need to have the correct volume V, are taken as snapshots from a regular $(N, P, \boldsymbol{\sigma}_a = \mathbf{0}, T)$ simulation. To generate these snapshots, the $(N, P, \boldsymbol{\sigma}_a = \mathbf{0}, T)$ simulation is started at a sufficiently large volume V_M and a sufficiently high external pressure P,

so that the structure will shrink, and reach a minimal volume V_m after sweeping through all volumes in $[V_m, V_M]$. If one is interested in an initial structure with unit cell volume $V \in [V_m, V_M]$, a snapshot of the system is taken with a unit cell volume V_i which is the closest to V, and differs by maximally 1 Å^3 for MIL-53(Al) and 2 Å^3 for MOF-5. Any remaining mismatch between V_i and V is removed by rescaling the unit cell tensor and the coordinates isotropically by a factor $(V/V_i)^{1/3}$. The volume grid spacing is chosen larger than 2 Å^3, so that two neighbouring volume grid points will always start from a different initial configuration.

A series of $(N, V, \boldsymbol{\sigma}_a = \mathbf{0}, T)$ simulations also leads to the determination of the bulk modulus, which gives information about the elasticity of the MOF. Different definitions are used throughout literature.[91–93] In this work, the bulk modulus K at a given volume V will be determined based on the monitored $\langle P_i \rangle$, following the relation

$$K(V) = -V \frac{\partial \langle P_i \rangle}{\partial V} \tag{2.12}$$

Here, $\langle P_i \rangle$ as a function of the volume is first fitted by means of a polynomial, so that the integration of Eq. (2.11) and the derivative of Eq. (2.12) can be carried out analytically, hence reducing the noise. The degree of the polynomial is always odd, in order to correctly describe the asymptotic behaviour of the free energy. The maximal polynomial degree is chosen such that no overfitting issues arise, i.e. the Vandermonde matrix corresponding to the fit cannot be rank-deficient.

3 Computational details

In this work, all MD simulations are carried out in either the $(N, P, \boldsymbol{\sigma}_a = \mathbf{0}, T)$ or the $(N, V, \boldsymbol{\sigma}_a = \mathbf{0}, T)$ ensemble, in which the number of particles is kept fixed, and the temperature as well as the deviatoric internal stress are controlled. Additionally, in the first ensemble, the average isotropic pressure is imposed to be constant, while the volume is kept

fixed in the second ensemble. All these simulations are carried out at a temperature of $T = 300$ K, using in-house developed force fields which contain covalent, electrostatic and van der Waals contributions.[94,95] These force fields have already shown their accuracy to reproduce geometrical properties of the two MOFs, MIL-53(Al) and MOF-5. Further details on the construction of the force fields can be found in Refs. 94 and 95.

In each of the simulations, the three barostats have been applied in turn and extended with the appropriate thermostat (the Berendsen thermostat, the Nosé-Hoover thermostat or the Langevin thermostat) with a relaxation time of 0.1 ps. (i) The MIL-53(Al) simulations are carried out with a Verlet timestep of 0.5 fs for a total simulation time of 800 ps, which turned out to be sufficient for the properties under study. For the barostat, the relaxation time is varied between 1 ps, 5 ps and 10 ps. A supercell obtained by aligning two unit cells in the direction of the shortest cell vector is considered, which contains a total of 152 atoms. A pressure profile for a supercell containing 304 atoms was also simulated, confirming that increasing the supercell does not influence the pressure profile appreciably. (ii) For MOF-5, the Verlet timestep can be increased to 0.75 fs due to the absence of the high-frequency O–H mode, and the total simulation time is 600 ps. Only one unit cell is considered, which already contains 424 atoms. The relaxation time constants are the same as for the MIL-53 simulations. VMD was used to visualise different snapshots of the simulations.[96]

For the initial structure of the $(N, P, \boldsymbol{\sigma}_a = \mathbf{0}, T)$ simulations, the equilibrium state at zero pressure and temperature is taken. The LP state was chosen for MIL-53(Al). For MIL-53(Al), simulations were carried out with a fixed isotropic pressure P between 100 kPa and 1 GPa in nine pressure steps. This broad pressure range is in accordance with the range required to fully characterise the flexible material, as mentioned in the introduction. For every pressure, 100 simulations were carried out for the MTTK and Langevin barostat. For the Berendsen barostat, 10 simulations proved to be sufficient to accurately determine the time to transition. The structural parameters for the LP phase of this material are averaged over the interval $[0, t_{\mathrm{LP}\to\mathrm{CP}} - 2\tau_P]$, while the CP phase averages are determined

based on the interval $[t_{\mathrm{LP}\to\mathrm{CP}} + 2\tau_P, t_{\mathrm{end}}]$. Here, $t_{\mathrm{LP}\to\mathrm{CP}}$ is the time to transition of Eq. (2.8) and t_{end} denotes the end of the simulation. To gather statistics inherent to the LP and CP states, a time span of $2\tau_P$ before and after the transition is cut out of the trajectory, as shown in Figure S.1. For MOF-5, the fixed isotropic pressure for each simulation is chosen between 100 kPa and 30 MPa in six pressure steps. Note that the highest pressures for MIL-53(Al) are not used here, since MOF-5 is much more rigid, and less variation in the simulated parameters is expected. To obtain the initial structures for the $(N, V, \boldsymbol{\sigma}_a = \mathbf{0}, T)$ simulations, the procedure as outlined in the Methodology section (Section 2.3.2) is followed. The computational parameters are unchanged with respect to the $(N, P, \boldsymbol{\sigma}_a = \mathbf{0}, T)$ ensemble simulations. For MOF-5, the unit cell volume takes values in the interval $[16915\ \text{Å}^3, 18615\ \text{Å}^3]$ with a step size of 10 Å^3, while for MIL-53(Al) the unit cell volume is comprised in the interval $[725\ \text{Å}^3, 1535\ \text{Å}^3]$ with a step size of 5 Å^3.

4 Results and Discussion

The different barostats and corresponding relaxation times will be tested on a variety of properties. In Section 4.1, we will discuss the geometry and stability of the closed-pore (CP) and the large-pore (LP) states of MIL-53(Al), as well as of the equilibrium state of MOF-5. The cell parameters will be determined, and compared with experiment. Moreover, for MIL-53(Al), internal coordinates will be defined that are shown to play an important role in the LP-to-CP transition.[59] In Section 4.2, the free energy profile will be derived for both materials, allowing to estimate the bulk moduli and transition pressures. The transition pressure can also be determined directly via a set of $(N, P, \boldsymbol{\sigma}_a = \mathbf{0}, T)$ simulations, which are performed in Section 4.3.

4.1 Characterisation of the stable and metastable states

4.1.1 Unit cell parameters of MIL-53(Al) and MOF-5

For the characterisation of the stable state of MOF-5 and the LP and CP states of MIL-53(Al), ten $(N, P, \boldsymbol{\sigma}_a = \mathbf{0}, T)$ simulations are carried out for the three different barostats with various barostat relaxation times τ_P. The resulting cell parameters (see Figure 3) are reported in Tables S.1–S.3 in the Supporting Information. In the case of MIL-53(Al), the b axis corresponds to the direction of the metal oxide chain. The MD simulations are carried out at 300 K and at different pressures varying between 100 kPa and 1 GPa. For each of the data points, the sampling error is calculated as the standard deviation for the ten simulations, which are assumed independent by choosing different initial conditions. The sampling error is smaller than 0.3 Å and is given in Tables S.1–S.3.

Figure 3 illustrates how the simulation results are hardly affected by the barostat relaxation time at 100 kPa, but are sensitive to the choice of the barostat. In all cases, the MTTK and Langevin results are comparable, while the Berendsen barostat deviates slightly in the particular case of MIL-53(Al) LP. The estimates of the a and c cell lengths differ from the other two barostats, as seen in Table S.1. The discrepancy amounts to a value of about 0.5–1.0 Å, and turns out to be three times larger than the largest standard deviation. These directions are the most flexible in the LP structure of MIL-53(Al), as was determined earlier by Ortiz *et al.*[97]

Moreover, as shown in Section 2.3 of the Supporting Information, both unit cell vectors are strongly coupled. A scatter plot of the cell lengths a and c in the LP phase during an $(N, P, \boldsymbol{\sigma}_a = \mathbf{0}, T)$ simulation shows that the free energy minimum area in the (a, c) plane, determined by the most frequently visited configurations, is characterised by an elongated, narrow region when using the MTTK and Langevin barostats (Fig. S.3). Due to the reduced pressure fluctuations, the Berendsen barostat converges only very slowly, explaining the observed difference in the predicted cell lengths for these soft directions. Increasing the sim-

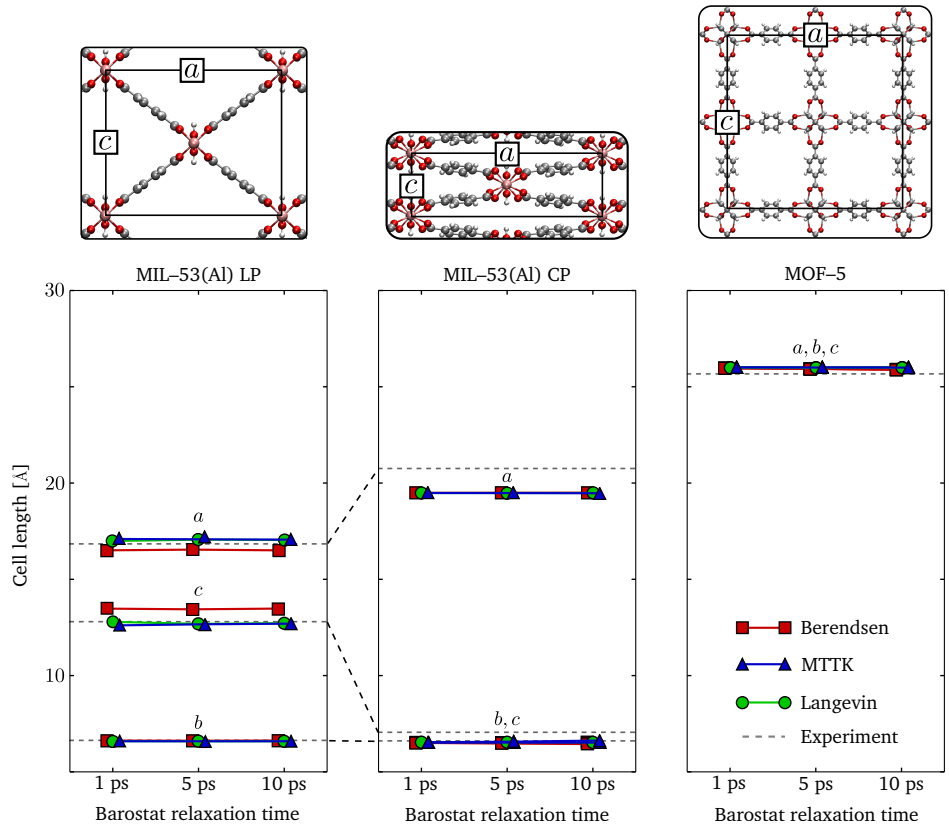

Figure 3: Cell parameters for the LP and CP states of MIL-53(Al) and the stable state of MOF-5 as averages from ten $(N, P, \boldsymbol{\sigma}_a = \mathbf{0}, T)$ simulations at 100 kPa and 300 K using the three barostats and for three relaxation times. The b axis of MIL-53(Al) corresponds to the direction of the metal oxide chain, while the other cell axes are introduced in the inset. Experimental values (dashed lines) are taken from Refs. 46 and 65, carried out at atmospheric pressure. The sampling errors on the cell parameters are very small (< 0.3 Å) and tabulated in Tables S.1–S.3 of the Supporting Information.

ulation time for the Berendsen barostat, however, does not yield an appropriate alternative due to other well-known artifacts of that barostat.[5,6]

$(N, P, \boldsymbol{\sigma}_a = \mathbf{0}, T)$ MD simulations at higher pressures, up to 1 GPa, were also carried out, leading to the same conclusions regarding the performance of the barostat and barostat relaxation time.

All cell lengths of the MIL-53(Al) LP and the MOF-5 equilibrium structure simulated with the MTTK and Langevin barostat coincide fairly well with the experimental estimates. Especially, these $(N, P, \boldsymbol{\sigma}_a = \mathbf{0}, T)$ simulations confirm the cubic structure (space group *Fm-*

3m) of MOF-5,[46] and yield the space group *Pmma* for the LP structure and *P2/c* for the CP structure of MIL-53(Al). These symmetry groups correspond to those found experimentally, when correcting for the fact that the simulated BDC linkers have a small and opposite tilting, which is not easy to observe via XRD due to the small reflectance of the carbon atoms, and the associated large error on their positions.[65] For the reproduction of the CP structure in MIL-53(Al), some deviation from experiment is noticed, but this is probably due to a force-field effect, as has been reported earlier.[94] A similar analysis, carried out for the cell angles α, β and γ, reveals that there is much less spread between the different barostats and barostat relaxation times, as shown in Tables S.1–S.3. As a consequence, the unit cell volume of the MIL-53(Al) LP phase is slightly overestimated by the Berendsen barostat (ca. 1470 Å^3), but is in agreement with experiment for the MTTK and Langevin barostats (1415–1430 Å^3). The predicted volumes for the stable phases, 814–834 Å^3 for the CP phase of MIL-53(Al) and 17364–17571 Å^3 for MOF-5, coincide for all barostats.

4.1.2 Internal coordinates characterising the LP → CP transition in MIL-53(Al)

Besides the cell parameters, which give an indication of the collective motion of the atoms, the LP-to-CP transition in MIL-53(Al) can also be characterised by the internal movement of a small, well-chosen set of atoms. In particular, two motions seem predominant in this transition: the O_CAlO_C angle and the AlO_CCC dihedral. The O_CAlO_C angle, shown in Figure 4, is the internal angle between the carboxylate oxygen-aluminium bonds of each of the four linkers. For each aluminium atom, there are hence four such angles exhibiting a magnitude around 90° in the LP phase. The AlO_CCC dihedral, shown in Figure 5, indicates a rotation of the phenyl linker with respect to the metal center about the O–O axis, which was found to act as a kneecap during the LP-to-CP transition.[98] Again, four such angles are found for each metal center. For this torsion angle, the IUPAC convention is used,[99] where the negative angles, in the range $[-180°, 0°]$, were translated to the interval $[180°, 360°]$, enabling a better visualisation of the results.

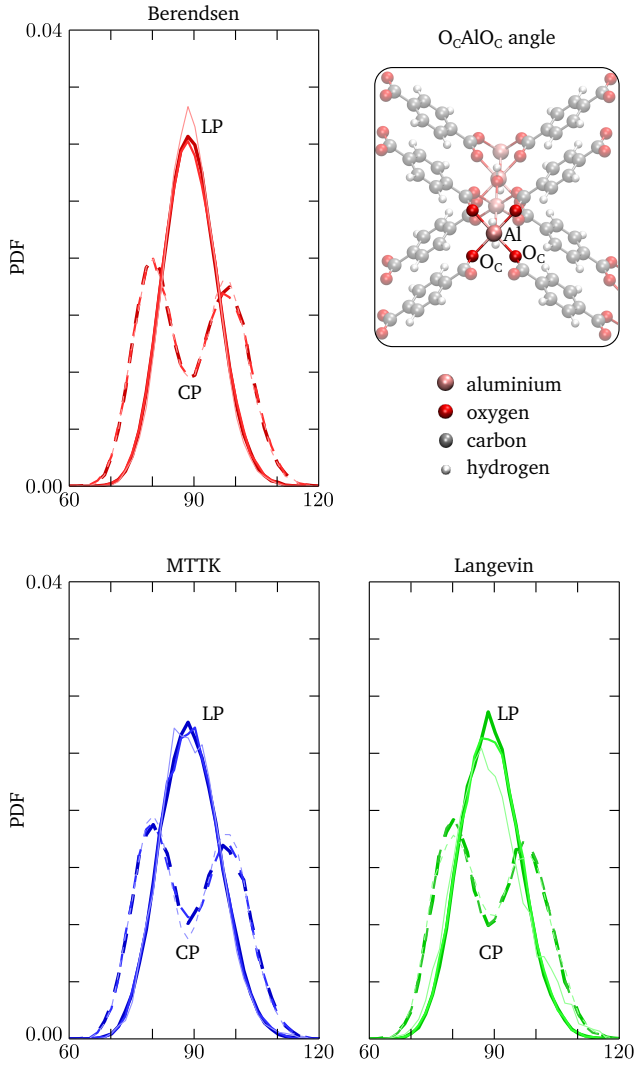

Figure 4: Probability density function (PDF), in $1/^\circ$ of the O_CAlO_C angles, in $^\circ$, present in the unit cell of MIL-53(Al) in both the large-pore (full line) and the closed-pore (dashed line) structure at 300 K and 1 MPa, using the three barostats and barostat relaxation times as indicated in the text. The darker the colour, the higher the barostat relaxation time $\tau_P \in [1\text{ ps}, 5\text{ ps}, 10\text{ ps}]$.

To investigate the change of these internal coordinates, $(N, P, \boldsymbol{\sigma}_a = \mathbf{0}, T)$ simulations at 300 K and a hydrostatic pressure of 1 MPa are carried out. For the MTTK and Langevin barostat, one simulation starting at the LP structure was sufficient to sample both the large pore and the closed pore extensively, since a transition to the CP structure was found about mid-way the simulations (see for instance Fig. S.1). For the Berendsen barostat, two simulations were carried out per relaxation time, one starting in the LP, and one in the CP

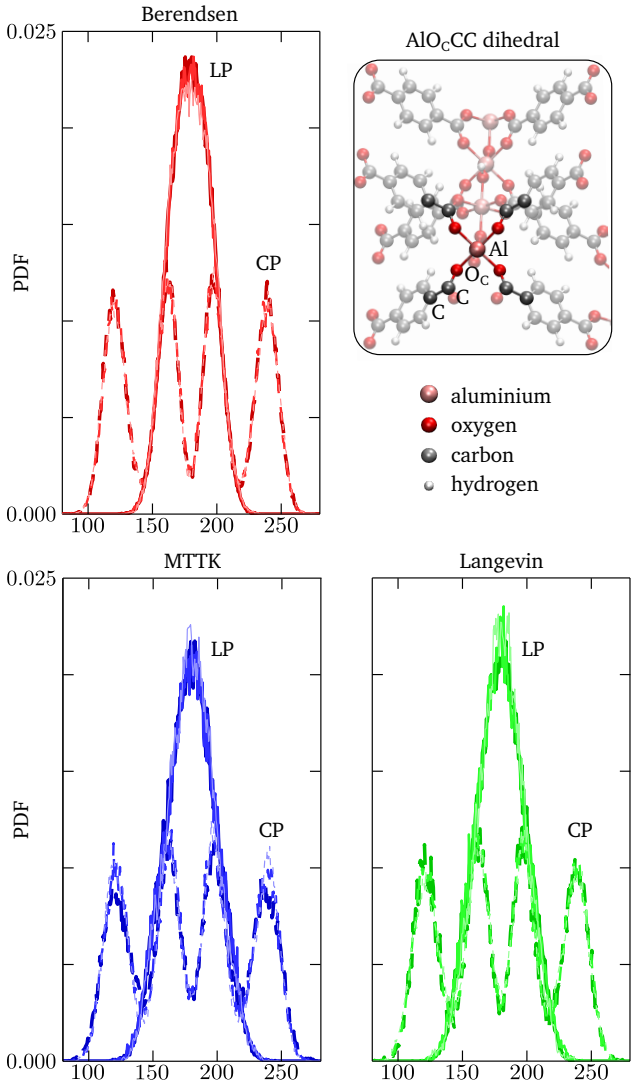

Figure 5: Probability density function (PDF), in 1/°, of the AlO_CCC dihedral angles, in °, present in the unit cell of MIL-53(Al) in both the large-pore (full line) and the closed-pore (dashed line) structure at 300 K and 1 MPa, using the three barostats and barostat relaxation times as indicated in the text. The darker the colour, the higher the barostat relaxation time $\tau_P \in [1\text{ ps}, 5\text{ ps}, 10\text{ ps}]$.

structure, since no LP-to-CP transition occurs at a pressure of 1 MPa.

For the O_CAlO_C angle, we deduce from Figure 4 that the LP-to-CP transition splits the 90° peak into two peaks, at 80° and 100°, separated by a valley in the probability density around 90°. This indicates that, upon transition to the CP structure, two of the phenyl linkers approach each other, decreasing their internal angle by 10°. This behaviour is

retrieved for each of the barostats and barostat relaxation times, with small deviations for the Berendsen barostat in the LP phase.

The AlO_CCC dihedral (Figure 5) also undergoes a distinct transformation during the LP-to-CP transition. While this torsion angle is peaked around 180° in the LP structure, the CP distribution function is dominated by four equidistant and equiprobable peaks, centered around 120°, 160°, 200° and 240°. This result shows symmetry with respect to 180°, as expected, and is in agreement with what has been reported in a recent work of Yot *et al.*[59] This splitting at the CP phase is independent of the barostat and barostat relaxation time. However, the LP peak is slightly narrower when using the Berendsen barostat, confirming once again that the Berendsen barostat does not exactly reproduce the results from the MTTK and Langevin barostat in the LP structure.

4.2 Free energy landscapes

Following the method outlined in the Methodology section, $(N, V, \boldsymbol{\sigma}_a = \mathbf{0}, T)$ simulations can be used to generate pressure and free energy profiles as a function of the unit cell volume for MIL-53(Al) and MOF-5. In Section 3.4 of the Supporting Information, we also included the free enthalpy profiles at different pressures, yielding an alternative method to follow the discussion below. From these profiles, one can deduce the stable and metastable states, as well as the transition pressures and bulk moduli. For all simulations reported in this section, the first 100 ps of the trajectories are regarded as an equilibration period, and properties are derived from the remaining 700 ps (MIL-53(Al)) or 500 ps (MOF-5).

4.2.1 Transition pressure for MIL-53(Al)

As was outlined previously, the $(N, V, \boldsymbol{\sigma}_a = \mathbf{0}, T)$ simulations allow to determine the average internal pressure $\langle P_i \rangle$, which is exerted by the material on its environment, as a function of the unit cell volume V. Subsequently, an eleventh-order polynomial $\langle P_i(V) \rangle$ is fitted to these results for MIL-53(Al) (see Table S.4). The simulations are performed for the three

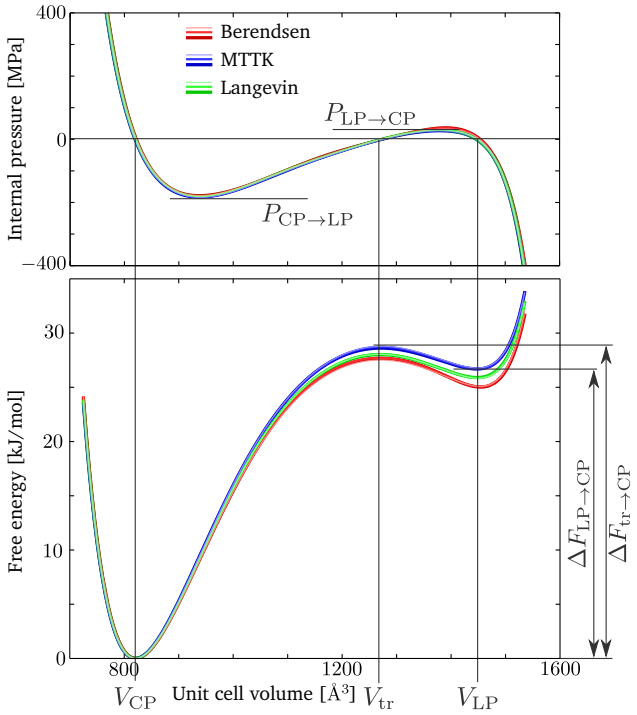

Figure 6: Fitted internal pressure P_i (top) and free energy F (bottom) profiles as a function of the constrained unit cell volume V for MIL-53(Al), resulting from $(N, V, \boldsymbol{\sigma}_a = \mathbf{0}, T)$ simulations at $T = 300$ K. For each barostat, three barostat relaxation times τ_P were considered: 1 ps, 5 ps and 10 ps, where the colour of the graph is darker the higher the relaxation time. For all barostats, the graphs coincide within the average error of the order of 1 MPa on the $P_i(V)$ plot and 0.05 kJ/mol on the $F(V)$ plot, as calculated via a bootstrap procedure (see S.I.). Simulated values of the equilibrium volumes, transition pressures, energy differences and bulk moduli are tabulated in Table S.6.

barostats and at three relaxation times τ_P: 1 ps, 5 ps and 10 ps. The $P_i(V)$ profiles are displayed in the upper pane of Figure 6.

All three barostats yield profiles which almost coincide with each other and which are independent of the chosen relaxation time within the sampling error. The pressure profile in the upper pane of Figure 6 also reveals the stable, and possibly metastable, structure(s) found at a given external pressure. The experimental measurements of the two phases in MIL-53(Al) took place at an external pressure of 100 kPa. According to our profile, three structures correspond to an external pressure of 100 kPa: the CP phase at V_{CP}, the LP phase at V_{LP}, and a transition point situated at V_{tr} that is unstable due to the positive derivative

$\partial P/\partial V$. In Section 3.4 of the Supporting Information, it is explicitly shown via a committor analysis that this unstable point indeed corresponds to a transition state.[100,101] The cell parameters of the transition state are given by $a = 18.3$ Å, $b = 6.5$ Å and $c = 10.7$ Å, and are hence in between the CP and LP states.

This pressure profile also predicts how the structures evolve when decreasing or increasing the external pressure, since in equilibrium the internal pressure equals the external pressure. The $P_i(V)$ graph shows two extrema: a minimum at $P_{\mathrm{CP}\rightarrow\mathrm{LP}}$ and a maximum at $P_{\mathrm{LP}\rightarrow\mathrm{CP}}$. In between these two pressures, one always encounters three structures (a transition state, a metastable and a stable state, as is clear from the free enthalpy profiles for these pressures, see Fig. S.6). For pressures above $P_{\mathrm{LP}\rightarrow\mathrm{CP}}$, only one stable state exists with a volume close to V_{CP}. In this pressure regime, the system remains in the closed pore, and the free enthalpy profile of Fig. S.6 indeed reveals only one minimum. Similarly, the system remains in the large pore for pressures below $P_{\mathrm{CP}\rightarrow\mathrm{LP}}$. An overview of the simulated values for the aforementioned volumes and transition pressures is reported in Table S.6.

Summarising, when starting from MIL-53(Al) in the LP phase at a pressure for which this phase is either stable or metastable, the volume of the material will systematically decrease with increasing pressure. Once the pressure reaches $P_{\mathrm{LP}\rightarrow\mathrm{CP}}$, the structure goes over from the metastable LP to the stable CP phase with a volume reduction of about 35% since the LP minimum in the free enthalpy disappears (see Fig. S.6). The material remains in this phase when further increasing the pressure. In Section 4.3, it will be discussed how fast this transition takes place. The reverse transformation occurs when starting from a CP structure at high pressures, for which it is again either stable or metastable. When systematically decreasing the external pressure, the material transforms from the metastable CP into the stable LP structure once the pressure reaches $P_{\mathrm{CP}\rightarrow\mathrm{LP}}$, corresponding to the disappearance of the free enthalpy minimum. Hence, for an external pressure in between these two transition pressures, the two phases may coexist as a stable and a metastable phase, and the phase observed during an experiment depends on the prior external conditions.[59] The pressure

profile hence indicates the existence of a hysteresis curve if negative pressures can be achieved experimentally. Negative pressures correspond to pulling the material isotropically, and may occur for instance when this MOF is embedded in a polymer film. More information on the occurrence of a particular phase and the transition among the various phases can be found in a recent paper of Vanduyfhuys *et al.* where a thermodynamic model was proposed to predict the conditions for phase transitions of flexible materials.[102,103]

The transition pressure $P_{\mathrm{CP}\rightarrow\mathrm{LP}}$ varies between -183 and -177 MPa, irrespective of the choice of barostat, while $P_{\mathrm{LP}\rightarrow\mathrm{CP}}$ varies between 27 and 30 MPa using the MTTK and Langevin barostat. These results for $P_{\mathrm{LP}\rightarrow\mathrm{CP}}$ are in good agreement with the experimental values of 13–18 MPa at 300 K.[59] The Berendsen barostat predicts a transition pressure $P_{\mathrm{LP}\rightarrow\mathrm{CP}}$ between 33 and 38 MPa, which deviates slightly from the results obtained with the other two barostats. This observation is in line with the results depicted in Figures 3–5, where only in the LP phase some deviation from the other two barostats is present. Note that the transition volume V_{tr} is about 1270 Å^3, instead of the ad hoc introduced value of 1000 Å^3 in Eq. (2.8). However, replacing this ad hoc value by the proper value of 1270 Å^3 to distinguish between the LP and CP phases does not significantly alter the time to transition $t_{\mathrm{LP}\rightarrow\mathrm{CP}}$, since the time the system spends in the transition region is small compared to the time spent in the (meta)stable states (see Fig. S.1).

4.2.2 Free energy landscapes and bulk moduli for MIL-53(Al) and MOF-5

By integrating the pressure profile according to Eq. (2.11), the free energy profiles for MIL-53(Al) and MOF-5, which are shown in Figure 6 (bottom) and Figure 7, are retrieved. For this integration, the CP volume is chosen as the reference volume for MIL-53(Al), while the equilibrium volume of MOF-5 is taken as the reference volume for this material.

The free energy profile of MIL-53(Al), displayed in the bottom pane of Figure 6, shows two minima corresponding to the closed-pore volume V_{CP} and the large-pore volume V_{LP}. The transition from the LP to the CP structure is slightly activated, prohibiting the LP

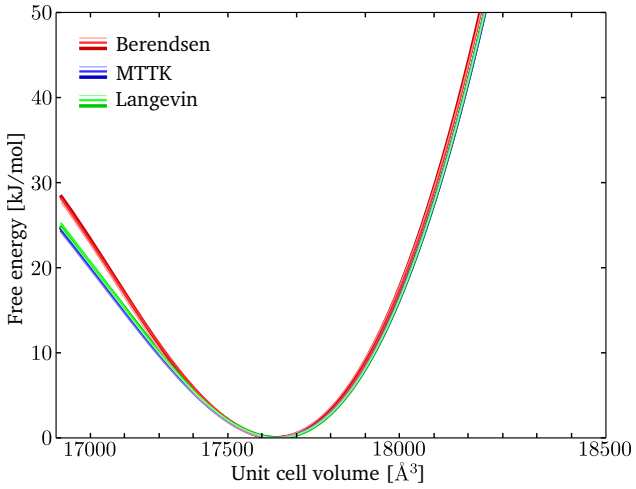

Figure 7: Free energy F as a function of the constrained unit cell volume V for MOF-5, resulting from $(N, V, \boldsymbol{\sigma}_a = \mathbf{0}, T)$ simulations at $T = 300$ K. For each barostat, three barostat relaxation times τ_P were considered: 1 ps, 5 ps and 10 ps, where the colour of the graph is darker the higher the relaxation time. The error on the free energy is of the order of 0.02 kJ/mol, as calculated via a bootstrap procedure (see S.I.). Simulated values of the equilibrium volume and bulk modulus are tabulated in Table S.7.

structure to shrink to the more deeply bound CP structure without external stimuli. Again, it is seen that the choice of the barostat relaxation time does not influence the free energy profile. A free energy difference between the CP and the LP states of 27.6–28.8 kJ/mol is predicted, while the barrier height amounts to 2.0–3.2 kJ/mol (with respect to the LP structure), depending on the barostat relaxation time. To the best of our knowledge, no experimental information is available on the free energy difference between these two phases, and only recently the internal energy difference was accessed experimentally.[104] For MOF-5, shown in Figure 7, similar conclusions can be drawn, where it is observed that all barostats nearly coincide within the given sampling error of 0.02 kJ/mol. For this material, a fifth-order polynomial fit of $\langle P_i \rangle$ as a function of V was carried out (see Table S.5).

As indicated in Eq. (2.12), the bulk modulus can be calculated based on the internal pressure profile. This calculation is carried out for the equilibrium structure of MOF-5 and the CP and LP states of MIL-53(Al) at 300 K, and tabulated in Tables S.6–S.7. For MOF-5, bulk moduli of 6.6 to 7.3 GPa are found. These values compare well with earlier

simulations, where bulk moduli in the range of 14.4 GPa to 20.0 GPa are reported near or at 0 K.[68,77,105–111] Force-field simulations furthermore show that the MOF-5 bulk modulus systematically decreases with increasing temperature, reducing to 4.0–16.66 GPa at 300 K.[108,109] For MIL-53(Al), the bulk modulus of the CP structure amounts to 3.33–3.66 GPa, while the LP structure yields a lower bulk modulus of 1.58–2.58 GPa, both calculated using the three barostats with different relaxation times. The lower bulk modulus for the LP structure confirms the intuition that the open structure is more easily compressed than the CP structure. Experimentally, a bulk modulus of 0.35 GPa for the LP phase at 300 K was reported by Yot *et al.*[59] Ongoing experiments in this research group indicate a CP bulk modulus of circa 10 GPa at 300 K.

When comparing the pressure distributions imposed by the different barostats in Figure 2, it was observed that the Berendsen barostat suppresses pressure fluctuations, and hence is unable to sample the isobaric ensembles exactly. As shown in Figure S.4, this leads to $(N, V, \boldsymbol{\sigma}_a = \mathbf{0}, T)$ simulations for which the Berendsen distribution of the cell parameters is much narrower than the MTTK and Langevin distributions, similar to the pressure and volume distributions during $(N, P, \boldsymbol{\sigma}_a = \mathbf{0}, T)$ simulations (see Figure 2). However, in the preceding discussion, the results obtained with the Berendsen barostat seem to agree well with the MTTK and Langevin results. This rather surprising result is explained based on the linear behaviour of the internal pressure as a function of the cell parameters, shown in Figure S.5. Due to this linearity, any symmetric distribution of the cell parameters with the correct mean will result in the same average internal pressure, explaining the coinciding results in Figure 6 and Figure 7. However, it is expected that the Berendsen results will vary appreciably when the properties under interest do no longer vary linearly. For instance, an alternative way to calculate the bulk modulus of a material is based on the following formula:[93]

$$K = k_B \langle T \rangle \frac{\langle V \rangle}{\langle V^2 \rangle - \langle V \rangle^2} \tag{4.1}$$

For MIL-53(Al), this bulk modulus is calculated based on the $(N, P, \boldsymbol{\sigma}_a = \mathbf{0}, T)$ trajectories

used to determine the distribution of the internal coordinates. Both the MTTK and Langevin barostats predict bulk moduli of 8.5–12.1 GPa (CP), respectively 3.2–10.1 GPa (LP) at 300 K. These bulk moduli are in agreement with the results obtained based on the pressure profile. However, when using the Berendsen barostat, much higher bulk moduli are predicted, amounting to 275–1150 GPa (CP) and 93–215 GPa (LP). These Berendsen results are one to two orders of magnitude higher than the results obtained with the other barostats, since the calculation of the bulk modulus explicitly depends on the volume fluctuations.

4.3 Determination of the transition pressure and time to transition for MIL-53(Al)

In the method outlined above, the transition pressure for MIL-53(Al) could be determined from the construction of a P_i versus V profile from a series of $(N, V, \boldsymbol{\sigma}_a = \mathbf{0}, T)$ simulations at different volumes. One can argue that one straightforward $(N, P, \boldsymbol{\sigma}_a = \mathbf{0}, T)$ simulation for a small set of pressures P will reveal the same information, while fewer simulations are needed. The idea is that, when we perform a simulation at a given pressure P and observe the system shrink from the LP to the CP structure, we assume that the pressure P of the simulation is higher than the mechanically required transition pressure $P_{\mathrm{LP}\rightarrow\mathrm{CP}}$. In contrast, if no transition is observed, it is assumed that the pressure P of the simulation is lower than the transition pressure $P_{\mathrm{LP}\rightarrow\mathrm{CP}}$. As such, one can—in principle—easily determine the transition pressure $P_{\mathrm{LP}\rightarrow\mathrm{CP}}$ by choosing a small set of well chosen pressures. Moreover, this method would also allow us to determine the time $t_{\mathrm{LP}\rightarrow\mathrm{CP}}$ the system needs to undergo this transition (Eq. 2.8). This could reveal new insights in the transition process, since to date, no experimental tools are able to capture this transition time as it occurs too fast. [112]

For the Berendsen barostat, we observe that the occurrence of a LP-to-CP transition within the simulation time of 800 ps at a certain pressure depends on the barostat relaxation time. For $\tau_P = 1$ ps, a pressure of 30 MPa suffices to steer the structure from the metastable large pore into the stable closed pore. Upon increasing this relaxation time to 5 ps, a

pressure of 1 GPa is needed, while no transition is seen for $P \leq 1$ GPa when using a relaxation time of 10 ps. Doubling the simulation time to 1.6 ns did not alter these findings. While the first result is in agreement with experimental observations predicting a transition pressure of 13–18 MPa,[59] it is clear that the dependence on relaxation time is unphysical, and should be avoided. For the MTTK and Langevin barostat, the time to transition $\bar{t}_{\mathrm{LP}\to\mathrm{CP}}$, averaged over 100 simulations, shows a completely different behaviour, as can be seen in the central pane of Figure 8. A LP-to-CP transition is observed for all pressures, including the low pressures to the left of the vertical line $P_{\mathrm{LP}\to\mathrm{CP},\mathrm{exp}}$ in this figure, in contrast to the experimental observations. Moreover, we observe that the average time to transition $\bar{t}_{\mathrm{LP}\to\mathrm{CP}}$ clearly increases when increasing the barostat relaxation time. Note that these average times to transition are relatively fast, independent of the relaxation time, supporting our choice to limit the total simulation time to 800 ps. This effect is not completely unexpected: the barostat relaxation time τ_P determines how fast the unit cell tensor $\mathbf{h}$, and hence the volume V, can respond upon external pressure stimuli, and will hence regulate the time it takes for the metastable or unstable LP structure to shrink to the stable CP phase. These results indicate that the barostat coupling method cannot be used to determine dynamic variables directly related to the movement of the unit cell tensor as a whole, such as this average time to transition, since it depends on the chosen barostat relaxation time.

However, in Section 4.2, we succeeded in determining the transition pressure, a static variable, from the free energy profile. The same information should be present in this dynamic characterisation, albeit possibly overshadowed by the interference of the barostats. To extract this information, we will rely on a statistical model to describe the transition, as outlined in Appendix A. For every given choice of barostat, barostat relaxation time and pressure, we determine whether the simulated time to transition can best be described using a Poisson model, mimicking rare events, or using a Gaussian model, corresponding to a spontaneous transition. We introduce the ratio R as the ratio of the likelihood that the process can be described by a Gaussian or a Poisson model.

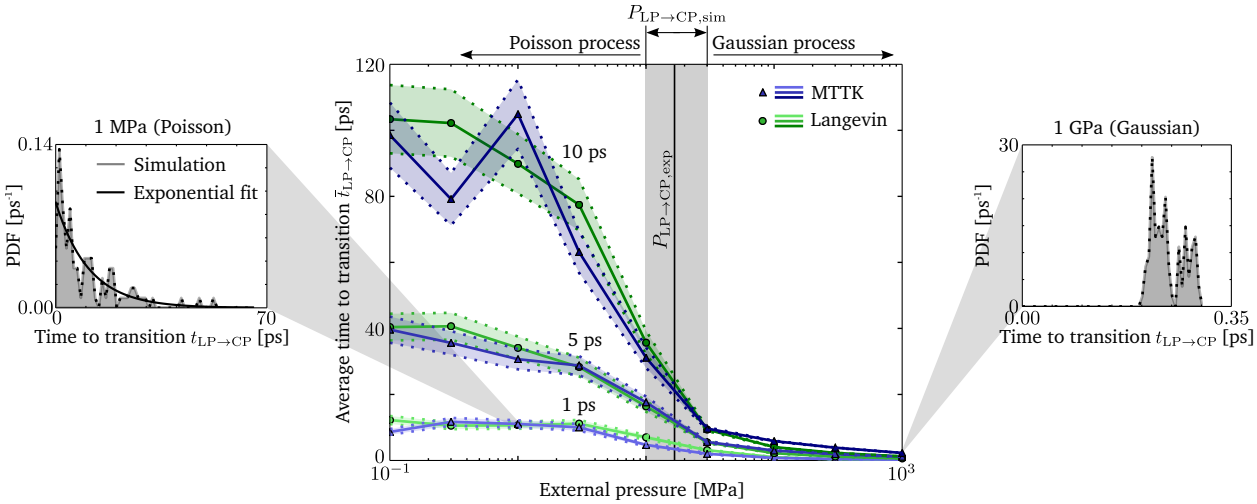

Figure 8: Average simulation time needed to observe the MIL-53(Al) LP-to-CP transition in a $(N, P, \boldsymbol{\sigma}_a = \mathbf{0}, T)$ ensemble at 300 K as a function of the applied pressure, carried out for different barostats and barostat relaxation times of 1 ps, 5 ps and 10 ps. The shaded regions indicate the 1σ confidence interval for this average simulation time (see Appendix and S.I.). Also indicated are the experimental transition pressure $P_{\mathrm{LP}\to\mathrm{CP,exp}}$ and the transition region $P_{\mathrm{LP}\to\mathrm{CP,sim}}$ predicted via our statistical analysis. In the side panes, the probability density function (PDF) for the time to transition is displayed for two selected pressures, and consists of 100 independent simulation results carried out with the MTTK barostat and a relaxation time of 1 ps. Other pressures are shown in Figure S.9 of the Supporting Information.

If we apply a large external pressure P, higher than the transition pressure, we expect that the system immediately adapts to this pressure, and shrinks early in the simulation to the CP phase (low $t_{\mathrm{LP}\to\mathrm{CP}}$). The only variation in this time to transition is due to different initial conditions, so that we can describe these high-pressure transitions as a Gaussian process. Furthermore, an increase in the applied pressure will increase the steering force, and hence decrease the observed time to transition. This is indeed observed in the high-pressure regime of Figure 8, extending from about 30 MPa, where the transition can be described by a Gaussian process, and is hence spontaneously occurring at these pressures. Also the large ratio $R \sim \exp(100)$ in Figure S.8 evidences this observation.

In contrast, if we apply an external pressure P much lower than the transition pressure, a LP-to-CP transition is not expected. However, we still observe a phase transformation during a $(N, P, \boldsymbol{\sigma}_a = \mathbf{0}, T)$ MD simulation at times much larger than in the high-pressure regime.

The large pressure fluctuations when using the Langevin and MTTK barostats, as observed in the left pane of Figure 2, cause this behaviour. It is expected that, at a certain point during the simulation, a sequence of pressure fluctuations will appear that have a sufficiently high positive amplitude to drive a LP-to-CP transition. This process yields a much larger time to transition since such a prolonged large pressure fluctuation is an infrequent event, consistent with a Poisson process. However, if the simulation time is sufficiently long, as is the case here, the LP-to-CP transition will certainly take place. As an example, we refer to Figure S.1 in the Supporting Information, in which the MIL-53(Al) unit cell volume is shown during an $(N, P, \boldsymbol{\sigma}_a = \mathbf{0}, T)$ simulation at 300 K and at a pressure of 1 MPa, lower than the LP-to-CP transition pressure. For the particular simulation displayed in Figure S.1, the time to transition $t_{\mathrm{LP}\rightarrow\mathrm{CP}}$ takes place at about 320 ps. This whole reasoning is built upon sufficiently large pressure amplitudes, which, for a given force field, can depend on the size of the simulation cell and the barostat properties. Experiment is not able to elucidate this process, since it occurs too fast.[112]

Moreover, since the pressure fluctuations at 300 K and at low pressures are dominated by temperature effects, these transitions are expected to be quasi independent of the applied external pressure, resulting in $\bar{t}_{\mathrm{LP}\rightarrow\mathrm{CP}}$ being fairly independent of P. This low-pressure behaviour is indeed observed in Figure 8, up to a pressure of about 10 MPa. Furthermore, Figure S.8 reveals that also the ratio $R \sim \exp(-80)$ in this pressure range, indicating a clear preference for the Poisson model. Moreover, these results are the same for the MTTK and Langevin barostat, and almost independent of the barostat relaxation time. When using the Berendsen barostat, pressure fluctuations are suppressed, so that this LP-to-CP transition will rarely occur within a feasible simulation time, as is indeed observed in our simulations.

Summarising, the $(N, P, \boldsymbol{\sigma}_a = \mathbf{0}, T)$ simulations allow to determine the LP-to-CP transition pressure (10–30 MPa), but fail to determine dynamic quantities which are directly related to cell fluctuations, as the system is perturbed by the barostat. Not only is this method less accurate than the $(N, V, \boldsymbol{\sigma}_a = \mathbf{0}, T)$ simulations of Section 4.2, it is also less

efficient. For the $(N, P, \boldsymbol{\sigma}_a = \mathbf{0}, T)$ simulations, a lot of trajectories (here: 100) are needed for every pressure to obtain reliable statistics, while for the $(N, V, \boldsymbol{\sigma}_a = \mathbf{0}, T)$ simulations, a few trajectories per volume grid point suffice to determine the $P_i(V)$ profile and its error.

5 Conclusions

In this work, we have compared three different barostat implementations, the Berendsen, MTTK and Langevin barostat, to predict static and dynamic properties of metal-organic frameworks. While the MTTK and Langevin pressure control schemes only differ by the introduction of a Brownian motion in the Langevin scheme, the Berendsen update scheme is completely different. The latter aims at an exponential damping of the difference between the instantaneous and externally applied pressure, hence disfavouring pressure fluctuations. As expected, this results in a pressure distribution that is much narrower than when using the MTTK or Langevin barostat, in agreement with earlier results for the Berendsen thermostat[87] and barostat.[9]

The effect of the barostat choice has been investigated with $(N, V, \boldsymbol{\sigma}_a = \mathbf{0}, T)$ and $(N, P, \boldsymbol{\sigma}_a = \mathbf{0}, T)$ MD simulations for two materials: the rigid MOF-5 and the flexible MIL-53(Al). First of all, for the large pore of MIL-53(Al) some of the cell length predictions of the Berendsen barostat slightly differ from the MTTK/Langevin and experimental results, even when taking into account the sampling error. Similar minor differences are seen for the internal coordinates playing a dominant role in the MIL-53(Al) LP-to-CP transition. Changing the barostat relaxation time does not influence these findings appreciably.

Second, a thermodynamic integration procedure was applied to derive the free energy as a function of volume for both MIL-53(Al) and MOF-5 at 300 K. Here, the results obtained with the three barostats coincide, independent of the barostat relaxation time. This is not in disagreement with the deviating shape distribution of the Berendsen barostat, due to the linear behaviour of the pressure as a function of the shape. However, for nonlinear functions,

such as used when calculating the bulk modulus based on the standard deviation of the volume fluctuations, the Berendsen results deviate. From the pressure versus volume curves, the transition pressures from the LP to the CP phase and vice versa are deduced. The experimental LP-to-CP transition pressure is 13–18 MPa at 300 K, which corresponds fairly well to the transition pressures derived from our simulations using the three barostats—only the Berendsen barostat shows some small deviations.

Third, we have investigated the transition pressures and the time to transition from the $(N, P, \boldsymbol{\sigma}_a = \mathbf{0}, T)$ simulations for MIL-53(Al). The time to shrink from the LP to the CP phase strongly depends on the barostat relaxation time, indicating that a barostat cannot be used to obtain dynamic parameters directly influenced by the cell movement. Nevertheless, we have been able to successfully derive the transition pressure from this type of simulations. For this, we have proposed a statistical criterion to distinguish between a Poisson-type transition (rare event) and a Gaussian-type transition (spontaneous event). For the LP-to-CP transition, the Poisson process is dominant for pressures lower than 10 MPa, while the Gaussian process dominates for pressures higher than 30 MPa, yielding a transition range of 10–30 MPa, in line with the experimental results. However, this method is less exact than thermodynamic integration, and would require more independent simulations to obtain the same accuracy.

In summary, while the Berendsen barostat can be efficiently used to equilibrate a system, it was shown that it should be used with caution when one wishes to obtain accurate results from MD simulations, especially when considering flexible materials. Moreover, we observed that both the MTTK and Langevin barostat yield the same results, and are in agreement with experimental results for the calculation of static variables. Hence, the choice between the MTTK and Langevin barostat is a matter of taste or necessity—for instance, only MTTK can be used when one needs to integrate the equations of motion backwards, e.g. as needed for transition path sampling.

Acknowledgement

This work is supported by the Fund for Scientific Research Flanders (FWO), the Research Board of Ghent University (BOF) and BELSPO in the frame of IAP/7/05. Funding was also received from the European Union's Horizon 2020 research and innovation programme [consolidator ERC grant agreement no. 647755 – DYNPOR (2015–2020)]. Computational resources (Stevin Supercomputer Infrastructure) and services were provided by Ghent University. We would also like to thank R. Demuynck, M. E. Tuckerman, M. Parrinello, Wm. G. Hoover, and C. G. Hoover for insightful and stimulating discussions.

Supporting Information Available

In the Supporting Information, we provide a Hamiltonian derivation of equations of motion implementing pressure coupling, as well as a tabular overview of simulated cell parameters and free energy landscapes. Furthermore, we include a derivation of the best estimators and their corresponding error for the two models explaining the LP-to-CP transition in MIL-53(Al). This material is available free of charge via the Internet at `http://pubs.acs.org/`.

A Statistical modeling of the LP-to-CP transition

In this Appendix, we will show how it is possible to classify the observed transitions from the large pore (LP) to the closed pore (CP) in MIL-53(Al) in either Gaussian- or Poisson-like processes, based on statistical considerations. For this, consider a simulation in which a LP-to-CP transition is observed after a given time to transition $t_{\mathrm{LP}\to\mathrm{CP}}$, as defined in Eq. (2.8). This time to transition potentially depends on the applied pressure, the type of barostat and the barostat relaxation time used to control this pressure. When comparing different simulations with the same barostat properties, it is observed that this time to transition $t_{\mathrm{LP}\to\mathrm{CP}}$ does not take a well-defined value for all simulations, but rather follows

an underlying distribution, defined by the process inducing the transition.

The first statistical model describes these LP-to-CP transitions as uncorrelated occurrences with a very low probability, so-called rare events. The transition can then be modelled as a Poisson process, and the corresponding time to transition is exponentially distributed. This distribution is completely defined by only one parameter t_0, the decay constant. In the Supporting Information, the estimator t_0^* is introduced as the value of t_0 which maximises the likelihood of the distribution,[113,114] which can be seen as the best estimator for t_0. As outlined in the Supporting Information, the 1σ confidence interval of t_0^*, given the uncorrelated data $\boldsymbol{X} = \{X_1, ..., X_N\}$ consisting of N observations, is

$$t_0^* = \overline{\boldsymbol{X}} \pm \frac{\overline{\boldsymbol{X}}}{\sqrt{N}}, \tag{A.1}$$

where $\overline{\boldsymbol{X}}$ denotes the sample mean.

In the second statistical model, the LP-to-CP transition is seen as a spontaneous event, and the corresponding times to transition are assumed to be distributed according to the Gaussian distribution, characterised by its mean μ and standard deviation σ. As outlined in the Supporting Information, the 1σ confidence intervals for these estimators are given by

$$\mu^* = \overline{\boldsymbol{X}} \pm \sqrt{\frac{s_{\boldsymbol{X}}^2}{N-1}} \tag{A.2}$$

and

$$\sigma^* = \sqrt{\frac{N}{N-1} s_{\boldsymbol{X}}^2} \pm \sqrt{\frac{N}{2(N-1)^2} s_{\boldsymbol{X}}^2} \tag{A.3}$$

where $s_{\boldsymbol{X}}^2 = \overline{\boldsymbol{X}^2} - \overline{\boldsymbol{X}}^2$ is the sample variance.

To determine which of both models agrees best with the given data, as obtained at a certain pressure and given the barostat and the barostat relaxation time, the ratio

$$R = \frac{\mathrm{prob}(G|\boldsymbol{X}, I)}{\mathrm{prob}(P|\boldsymbol{X}, I)} \tag{A.4}$$

is used as criterion. Here, the numerator prob$(G|\boldsymbol{X}, I)$ expresses the probability that the data can be explained by the Gaussian model, while the denominator prob$(P|\boldsymbol{X}, I)$ expresses the probability that the data can be explained by the Poisson model. If $R > 1$, the data supports the Gaussian model, while if $R < 1$, the Poisson model is preferred. The preference for one model over another, based on the relative magnitude of the applied pressure and the LP-to-CP transition pressure, is employed in the dynamical treatment of Section 4.3.

References

(1) Düren, T.; Bae, Y.-S.; Snurr, R. Q. *Chem. Soc. Rev.* **2009**, *38*, 1237–1247.

(2) Karplus, M.; McCammon, J. A. *Nat. Struct. Biol.* **2002**, *9*, 646–652.

(3) Tuckerman, M. E.; Martyna, G. J. *J. Phys. Chem. B* **2000**, *104*, 159–178.

(4) Alder, B. J.; Wainwright, T. E. *J. Chem. Phys.* **1959**, *31*, 459–466.

(5) Harvey, S. C.; Tan, R. K.-Z.; Cheatham, T. E. *J. Comput. Chem.* **1998**, *19*, 726–740.

(6) Chiu, S.; Clark, M.; Subramaniam, S.; Jakobsson, E. *J. Comput. Chem.* **2000**, *21*, 121–131.

(7) Page, A. J.; Isomoto, T.; Knaup, J. M.; Irle, S.; Morokuma, K. *J. Chem. Theory Comput.* **2012**, *8*, 4019–4028.

(8) Basconi, J. E.; Shirts, M. R. *J. Chem. Theory Comput.* **2013**, *9*, 2887–2899.

(9) Feller, S. E.; Zhang, Y.; Pastor, R. W.; Brooks, B. R. *J. Chem. Phys.* **1995**, *103*, 4613–4621.

(10) Turq, P.; Lantelme, F.; Friedman, H. *J. Chem. Phys.* **1977**, *66*, 3039–3044.

(11) Bussi, G.; Donadio, D.; Parrinello, M. *J. Chem. Phys.* **2007**, *126*, 014101.

(12) Bussi, G.; Parrinello, M. *Phys. Rev. E* **2007**, *75*, 056707.

(13) Bussi, G.; Parrinello, M. *Comput. Phys. Commun.* **2008**, *179*, 26–29.

(14) Bussi, G.; Zykova-Timan, T.; Parrinello, M. *J. Chem. Phys.* **2009**, *130*, 074101.

(15) Ceriotti, M.; Bussi, G.; Parrinello, M. *Phys. Rev. Lett.* **2009**, *102*, 020601.

(16) Ceriotti, M.; Parrinello, M. *Procedia Comput. Sci.* **2010**, *1*, 1607–1614.

(17) Ceriotti, M.; Bussi, G.; Parrinello, M. *J. Chem. Theory Comput.* **2010**, *6*, 1170–1180.

(18) Andersen, H. C. *J. Chem. Phys.* **1980**, *72*, 2384–2393.

(19) Berendsen, H. J. C.; Postma, J. P. M.; van Gunsteren, W. F.; Dinola, A.; Haak, J. R. *J. Chem. Phys.* **1984**, *81*, 3684–3690.

(20) Hoover, W. G.; Ladd, A. J. C.; Moran, B. *Phys. Rev. Lett.* **1982**, *48*, 1818–1820.

(21) Evans, D. J.; Morriss, G. P. *Chem. Phys.* **1983**, *77*, 63–66.

(22) Haile, J. M.; Gupta, S. *J. Chem. Phys.* **1983**, *79*, 3067–3076.

(23) Nosé, S. *Mol. Phys.* **1984**, *52*, 255–268.

(24) Nosé, S. *J. Chem. Phys.* **1984**, *81*, 511–519.

(25) Hoover, W. G. *Phys. Rev. A* **1985**, *31*, 1695–1697.

(26) Nosé, S. *Mol. Phys.* **1986**, *57*, 187–191.

(27) Martyna, G. J.; Klein, M. L.; Tuckerman, M. E. *J. Chem. Phys.* **1992**, *97*, 2635–2643.

(28) Morishita, T. *Mol. Phys.* **2010**, *108*, 1337–1347.

(29) Soddemann, T.; Dünweg, B.; Kremer, K. *Phys. Rev. E* **2003**, *68*, 046702.

(30) Campisi, M.; Hänggi, P. *J. Phys. Chem. B* **2013**, *117*, 12829–12835.

(31) Patra, P. K.; Bhattacharya, B. *J. Chem. Phys.* **2014**, *140*, 064106.

(32) Parrinello, M.; Rahman, A. *Phys. Rev. Lett.* **1980**, *45*, 1196–1199.

(33) Parrinello, M.; Rahman, A. *J. Appl. Phys.* **1981**, *52*, 7182–7190.

(34) Nosé, S.; Klein, M. L. *Mol. Phys.* **1983**, *50*, 1055–1076.

(35) Wentzcovitch, R. M. *Phys. Rev. B* **1991**, *44*, 2358–2361.

(36) Lill, J. V.; Broughton, J. Q. *Phys. Rev. B* **1992**, *46*, 73832–12071.

(37) Hoover, W. G. *Phys. Rev. A* **1986**, *34*, 2499–2500.

(38) Melchionna, S.; Ciccotti, G.; Holian, B. L. *Mol. Phys.* **1993**, *78*, 533–544.

(39) Martyna, G. J.; Tobias, D. J.; Klein, M. L. *J. Chem. Phys.* **1994**, *101*, 4177–4189.

(40) Martyna, G. J.; Tuckerman, M. E.; Tobias, D. J.; Klein, M. L. *Mol. Phys.* **1996**, *87*, 1117–1157.

(41) Quigley, D.; Probert, M. I. J. *J. Chem. Phys.* **2004**, *120*, 11432–11441.

(42) Zhou, H.-C.; Long, J. R.; Yaghi, O. *Chem. Rev.* **2012**, *112*, 673–674.

(43) Rowsell, J. L. C.; Millward, A. R.; Park, K. S.; Yaghi, O. M. *J. Am. Chem. Soc.* **2004**, *126*, 5666–5667.

(44) Gascon, J.; Hernández-Alonso, M.; Almeida, A.; van Klink, G.; Kapteijn, F.; Mul, G. *ChemSusChem* **2008**, *1*, 981–983.

(45) Biswas, S.; Vanpoucke, D. E. P.; Verstraelen, T.; Vandichel, M.; Couck, S.; Leus, K.; Liu, Y.-Y.; Waroquier, M.; Van Speybroeck, V.; Denayer, J. F. M.; Van Der Voort, P. *J. Phys. Chem. C* **2013**, *117*, 22784–22796.

(46) Li, H.; Eddaoudi, M.; O'Keeffe, M.; Yaghi, O. M. *Nature* **1999**, *402*, 276–279.

(47) Eddaoudi, M.; Kim, J.; Rosi, N.; Vodak, D.; Wachter, J.; O'Keeffe, M.; Yaghi, O. *Science* **2002**, *295*, 469–472.

(48) Long, J. R.; Yaghi, O. M. *Chem. Soc. Rev.* **2009**, *38*, 1213–1214.

(49) Kitagawa, S.; Kitaura, R.; Noro, S.-i. *Angew. Chem., Int. Ed.* **2004**, *43*, 2334–2375.

(50) Kitagawa, S.; Noro, S.-i.; Nakamura, T. *Chem. Commun.* **2006**, 701–707.

(51) Trung, T. K.; Trens, P.; Tanchoux, N.; Bourrelly, S.; Llewellyn, P. L.; Loera-Serna, S.; Serre, C.; Loiseau, T.; Fajula, F.; Férey, G. *J. Am. Chem. Soc.* **2008**, *130*, 16926–16932.

(52) Tranchemontagne, D. J.; Mendoza-Cortés, J. L.; O'Keeffe, M.; Yaghi, O. M. *Chem. Soc. Rev.* **2009**, *38*, 1257–1283.

(53) Perry IV, J. J.; Perman, J. A.; Zaworotko, M. J. *Chem. Soc. Rev.* **2009**, *38*, 1400–1417.

(54) Meek, S. T.; Greathouse, J. A.; Allendorf, M. D. *Adv. Mater.* **2011**, *23*, 249–267.

(55) Férey, G.; Serre, C. *Chem. Soc. Rev.* **2009**, *38*, 1380–1399.

(56) Férey, G.; Serre, C.; Devic, T.; Maurin, G.; Jobic, H.; Llewellyn, P. L.; De Weireld, G.; Vimont, A.; Daturi, M.; Chang, J.-S. *Chem. Soc. Rev.* **2011**, *40*, 550–562.

(57) Schneemann, A.; Bon, V.; Schwedler, I.; Senkovska, I.; Kaskel, S.; Fischer, R. A. *Chem. Soc. Rev.* **2014**, *43*, 6062–6096.

(58) Bazer-Bachi, D.; Assié, L.; Lecocq, V.; Harbuzaru, B.; Falk, V. *Powder Technol.* **2014**, *255*, 52–59.

(59) Yot, P. G.; Boudene, Z.; Macia, J.; Granier, D.; Vanduyfhuys, L.; Verstraelen, T.; Van Speybroeck, V.; Devic, T.; Serre, C.; Férey, G.; Stock, N.; Maurin, G. *Chem. Commun.* **2014**, *50*, 9462–9464.

(60) Gagnon, K. J.; Beavers, C. M.; Clearfield, A. *J. Am. Chem. Soc.* **2013**, *135*, 1252–1255.

(61) Ortiz, G.; Nouali, H.; Marichal, C.; Chaplais, G.; Patarin, J. *Phys. Chem. Chem. Phys.* **2013**, *15*, 4888–4891.

(62) Yot, P. G.; Ma, Q.; Haines, J.; Yang, Q.; Ghoufi, A.; Devic, T.; Serre, C.; Dmitriev, V.; Férey, G.; Zhong, C.; Maurin, G. *Chem. Sci.* **2012**, *3*, 1100–1104.

(63) Ma, Q.; Yang, Q.; Ghoufi, A.; Férey, G.; Zhong, C.; Maurin, G. *Dalton Trans.* **2012**, *41*, 3915–3919.

(64) Ghoufi, A.; Subercaze, A.; Ma, Q.; Yot, P. G.; Ke, Y.; Puente-Orench, I.; Devic, T.; Guillerm, V.; Zhong, C.; Serre, C.; Férey, G.; Maurin, G. *J. Phys. Chem. C* **2012**, *116*, 13289–13295.

(65) Liu, Y.; Her, J.-H.; Dailly, A.; Ramirez-Cuesta, A. J.; Neumann, D. A.; Brown, C. M. *J. Am. Chem. Soc.* **2008**, *130*, 11813–11818.

(66) Beurroies, I.; Boulhout, M.; Llewellyn, P. L.; Kuchta, B.; Férey, G.; Serre, C.; Denoyel, R. *Angew. Chem., Int. Ed.* **2010**, *122*, 7688–7691.

(67) Rowsell, J. L. C.; Spencer, E. C.; Eckert, J.; Howard, J. A. K.; Yaghi, O. M. *Science* **2005**, *309*, 1350–1354.

(68) Bahr, D.; Reid, J.; Mook, W.; Bauer, C.; Stumpf, R.; Skulan, A.; Moody, N.; Simmons, B.; Shindel, M.; Allendorf, M. *Phys. Rev. B* **2007**, *76*, 184106.

(69) Tan, J. C.; Cheetham, A. K. *Chem. Soc. Rev.* **2011**, *40*, 1059–1080.

(70) Ford, D. C.; Dubbeldam, D.; Snurr, R. Q.; Künzel, V.; Wehring, M.; Stallmach, F.; Kärger, J.; Müller, U. *J. Phys. Chem. Lett.* **2012**, *3*, 930–933.

(71) Rosenbach, N.; Jobic, H.; Ghoufi, A.; Salles, F.; Maurin, G.; Bourrelly, S.; Llewellyn, P.; Devic, T.; Serre, C.; Férey, G. *Angew. Chem., Int. Ed.* **2008**, *47*, 6611–6615.

(72) Rosenbach, N.; Jobic, H.; Ghoufi, A.; Devic, T.; Koza, M. M.; Ramsahye, N.; Mota, C. J.; Serre, C.; Maurin, G. *J. Phys. Chem. C* **2014**, *118*, 14471–14477.

(73) Babarao, R.; Jiang, J. *Langmuir* **2008**, *24*, 5474–5484.

(74) Salles, F.; Jobic, H.; Ghoufi, A.; Llewellyn, P. L.; Serre, C.; Bourrelly, S.; Férey, G.; Maurin, G. *Angew. Chem., Int. Ed.* **2009**, *121*, 8485–8489.

(75) Paesani, F. *J. Phys. Chem. C* **2013**, *117*, 19508–19516.

(76) Greathouse, J. A.; Allendorf, M. D. *J. Am. Chem. Soc.* **2006**, *128*, 10678–10679.

(77) Tafipolsky, M.; Schmid, R. *J. Phys. Chem. B* **2009**, *113*, 1341–1352.

(78) Ghoufi, A.; Maurin, G. *J. Phys. Chem. C* **2010**, *114*, 6496–6502.

(79) Tadmor, E. B.; Miller, R. E. *Modeling Materials: Continuum, Atomistic and Multiscale Techniques*; Cambridge University Press: Cambridge, 2011; pp 57–58.

(80) Todorov, I. T.; Smith, W.; Trachenko, K.; Dove, M. T. *J. Mater. Chem.* **2006**, *16*, 1911–1918.

(81) Plimpton, S. *J. Comput. Phys.* **1995**, *117*, 1–19.

(82) VandeVondele, J.; Krack, M.; Mohamed, F.; Parrinello, M.; Chassaing, T.; Hutter, J. *Comput. Phys. Commun.* **2005**, *167*, 103–128.

(83) Verstraelen, T.; Vanduyfhuys, L.; Vandenbrande, S.; Rogge, S. M. J. *Yaff, yet another force field*, http://molmod.ugent.be/software/.

(84) Holian, B. L.; De Groot, A. J.; Hoover, W. G.; Hoover, C. G. *Phys. Rev. A* **1990**, *41*, 4552–4553.

(85) Toxvaerd, S. *Mol. Phys.* **1991**, *72*, 159–168.

(86) Lippert, R. A.; Predescu, C.; Ierardi, D. J.; Mackenzie, K. M.; Eastwood, M. P.; Dror, R. O.; Shaw, D. E. *J. Chem. Phys.* **2013**, *139*, 164106.

(87) Morishita, T. *J. Chem. Phys.* **2000**, *113*, 2976–2982.

(88) Tuckerman, M. E.; Liu, Y.; Ciccotti, G.; Martyna, G. J. *J. Chem. Phys.* **2001**, *115*, 1678–1702.

(89) du Bourg, L. B.; Ortiz, A. U.; Boutin, A.; Coudert, F.-X. *APL Mater.* **2014**, *2*, 124110.

(90) Kirkwood, J. G. *J. Chem. Phys.* **1935**, *3*, 300–313.

(91) Kittel, C. *Introduction to Solid State Physics*, 8th ed.; John Wiley & Sons, Inc., 2005; pp 80–81.

(92) Hill, R. *Proc. Phys. Soc.* **1952**, *65*, 349–354.

(93) Landau, L. D.; Lifshitz, E. *Statistical Physics, Part 1*, 3rd ed.; Elsevier: Oxford, 1980; pp 338–345.

(94) Vanduyfhuys, L.; Verstraelen, T.; Vandichel, M.; Waroquier, M.; Van Speybroeck, V. *J. Chem. Theory Comput.* **2012**, *8*, 3217–3231.

(95) Vanduyfhuys, L.; Vandenbrande, S.; Verstraelen, T.; Schmid, R.; Waroquier, M.; Van Speybroeck, V. *J. Comput. Chem.* **2015**, *36*, 1015–1027.

(96) Humphrey, W.; Dalke, A.; Schulten, K. *J. Mol. Graphics* **1996**, *14*, 32–38.

(97) Ortiz, A. U.; Boutin, A.; Fuchs, A. H.; Coudert, F.-X. *Phys. Rev. Lett.* **2012**, *109*, 195502.

(98) Serre, C.; Bourrelly, S.; Vimont, A.; Ramsahye, N.; Maurin, G.; Llewellyn, P.; Daturi, M.; Filinchuk, Y.; Leynaud, O.; Barnes, P.; Férey, G. *Adv. Mater.* **2007**, *19*, 2246–2251.

(99) IUPAC Gold Book, *Torsion angle*, http://http://goldbook.iupac.org/T06406.html.

(100) Bolhuis, P. G.; Chandler, D.; Dellago, C.; Geissler, P. L. *Annu. Rev. Phys. Chem.* **2002**, *53*, 291–318.

(101) E, W.; Vanden-Eijnden, E. *J. Stat. Phys.* **2006**, *123*, 503–523.

(102) Ghysels, A.; Vanduyfhuys, L.; Vandichel, M.; Waroquier, M.; Van Speybroeck, V.; Smit, B. *J. Phys. Chem. C* **2013**, *117*, 11540–11554.

(103) Vanduyfhuys, L.; Ghysels, A.; Rogge, S. M. J.; Demuynck, R.; Van Speybroeck, V. *Mol. Simulat.* **2015**, *41*, 1311–1328.

(104) Rodriguez, J.; Beurroies, I.; Loiseau, T.; Denoyel, R.; Llewellyn, P. L. *Angew. Chem., Int. Ed.* **2015**, *54*, 4626–4630.

(105) Samanta, A.; Furuta, T.; Li, J. *J. Chem. Phys.* **2006**, *125*, 084714.

(106) Mattesini, M.; Soler, J.; Ynduráin, F. *Phys. Rev. B* **2006**, *73*, 094111.

(107) Zhou, W.; Yildirim, T. *Phys. Rev. B* **2006**, *74*, 180301.

(108) Han, S. S.; Goddard, W. A. *J. Phys. Chem. C* **2007**, *111*, 15185–15191.

(109) Greathouse, J. A.; Allendorf, M. D. *J. Phys. Chem. C* **2008**, *112*, 5795–5802.

(110) Yang, L.-M.; Vajeeston, P.; Ravindran, P.; Fjellvåg, H.; Tilset, M. *Inorg. Chem.* **2010**, *49*, 10283–10290.

(111) Lukose, B.; Supronowicz, B.; St. Petkov, P.; Frenzel, J.; Kuc, A. B.; Seifert, G.; Vayssilov, G. N.; Heine, T. *Phys. Status Solidi B* **2012**, *249*, 335–342.

(112) Ghoufi, A.; Maurin, G.; Férey, G. *J. Phys. Chem. Lett.* **2010**, *1*, 2810–2815.

(113) Jaynes, E. T. *Phys. Rev.* **1957**, *106*, 620–630.

(114) Jaynes, E. T. *Phys. Rev.* **1957**, *108*, 171–190.

Graphical TOC Entry